Equilibrium kinetic theory of weakly anisotropic embedded thin current sheets

M. I. Sitnov[1], **H. Arnold**[1]

[1]The Johns Hopkins University Applied Physics Laboratory, Laurel, Maryland, USA.

Key Points:

- Kinetic equilibria of ion-scale current sheets embedded into a thicker weakly anisotropic Harris-like current sheet are investigated
- The current density increase due to quasi-adiabatic ion motions may be substantial in spite of weak plasma anisotropy
- 2D thin current sheets have aspect ratios consistent with observations and controlled by the embedding strength

Corresponding author: M. I. Sitnov, Mikhail.Sitnov@jhuapl.edu

Abstract

Statistical and case studies, as well as data-mining reconstructions suggest that the magnetotail current in the substorm growth phase has a multiscale structure with a thin ion-scale current sheet embedded into a much thicker sheet. This multiscale structure may be critically important for the tail stability and onset conditions for magnetospheric substorms. The observed thin current sheets are found to be too long to be explained by the models with isotropic plasmas. At the same time, plasma observations reveal only weak field-aligned anisotropy of the ion species, whereas the anisotropic electron contribution is insufficient to explain the force balance discrepancy. Here we elaborate a self-consistent equilibrium theory of multiscale current sheets, which differs from conventional isotropic models by weak ion anisotropy outside the sheet and agyrotropy caused by quasi-adiabatic ion orbits inside the sheet. It is shown that, in spite of weak anisotropy, the current density perturbation may be quite strong and localized on the scale of the figure-of-eight ion orbits. The magnetic field, current and plasma density in the limit of weak field-aligned ion anisotropy and strong current sheet embedding, when the ion scale thin current sheet is nested in a much thicker Harris-like current sheet, are investigated and presented in an analytical form making it possible to describe the multiscale equilibrium in sharply stretched 2-D magnetic field configurations and to use it in kinetic simulations and stability analysis.

Plain Language Summary

Conventional kinetic equilibria with isotropic pressures for ions and electrons aimed to describe the current sheet in Earth's magnetotail cannot reproduce its multiscale structure with the proton gyroradius-scale current sheet being embedded into a much thicker sheet. They cannot explain either the formation of such thin current sheets sufficiently far from Earth. The embedding effect can be reproduced in case of anisotropic and agyrotropic plasmas because orbits of weakly magnetized ions near the current sheet deviate from the Larmor circle and become more like a figure of eight. However, the corresponding multiscale current sheet models have been studied so far for substantial and strong plasma anisotropy, while observations suggest that the tail plasmas are weakly anisotropic. Here we perform an analysis of a weakly anisotropic current sheet model, which transforms in the isotropic limit into a classical Harris sheet model, and show that the key observed embedding features can be reproduced.

1 Introduction

Earth's magnetotail is a key region of the magnetosphere, where the energy coming from its interaction with the solar wind is accumulated and then explosively released during substorms (Angelopoulos et al., 2013; M. Sitnov et al., 2019). The energy release involves processes on many scales from MHD to that of the electron gyroradius (Merkin et al., 2019; Stephens et al., 2019; Torbert et al., 2018). Therefore, first-principles investigations require kinetic approaches, including stability analysis (Hesse & Schindler, 2001; Pritchett & Coroniti, 2010; M. I. Sitnov & Schindler, 2010) and full particle-in-cell (PIC) simulations of the tail current sheet (CS) (Hesse & Schindler, 2001; Pritchett & Coroniti, 2010; Liu et al., 2014; M. I. Sitnov et al., 2013, 2014; Bessho & Bhattacharjee, 2014; Pritchett, 2015). A fundamental problem here is that the available selfconsistent CS equilibrium models, used to start the kinetic stability analysis or simulations, are often grossly inconsistent with observations. The most popular class of isotropic plasma models (Schindler, 1972) represent 2-D generalizations of the 1-D Harris model (Harris, 1962). In these models the magnetic field tension is balanced by the pressure gradient $\nabla p = \mathbf{j} \times \mathbf{B}$, where $\mathbf{B}$ is the magnetic field and $\mathbf{j} = \nabla \times \mathbf{B}$ is the electric current. However, the resulting relation between the CS aspect ratio L_x/L_z, where L_z is the CS half-thickness and L_x its inhomogeneity scale along the X-axis (the GSM coordinate system is used here), and

the magnetic field stretching factor $B_0/B_z \sim L_x/L_z$, where B_z and B_0 are the normal magnetic field at $z = 0$ and the lobe magnetic field $B_0 \approx B_x(|z| \gg L_z)$ (Cole & Schindler, 1972; Rich et al., 1972) is strongly violated, especially in the substorm growth phase. Observations show that CSs are too thin and elongated in terms of their current and (inverse) pressure gradient, compared to their field line stretching: $L_x/L_z \gg B_0/B_z$ or $|\nabla p| \ll |\mathbf{j} \times \mathbf{B}|$ (Artemyev et al., 2015, 2016; M. I. Sitnov et al., 2019).

The isotropic force balance violation is accompanied and likely related to the buildup of the multiscale CS structure in the substorm growth phase with the ion-scale thin CS (TCS) embedded into a much thicker current sheet (V. A. Sergeev et al., 1993; Runov et al., 2005; Runov et al., 2006; V. A. Sergeev et al., 2011). Most recently, the buildup and decay of a TCS inside a much thicker CS during substorms and its role in the violation of the isotropic force balance have been shown in the data-mining analysis of the geomagnetic field (M. I. Sitnov et al., 2019)

The multiscale structure of the tail CS and its deviation from classical Harris-type equilibria may therefore be critically important for the onset conditions for magnetospheric substorms and the underlying CS destabilization mechanisms. The main candidates for the destabilization are the electron (Coppi et al., 1966) and ion (Schindler, 1974; Galeev & Zelenyi, 1976) tearing modes providing the onset of magnetic reconnection. The main impediment is the almost universal tearing stability of the tail CS as long as electrons are magnetized by the equatorial magnetic field B_z (Lembege & Pellat, 1982; Pellat et al., 1991) and the latter is not increasing tailward (M. I. Sitnov & Schindler, 2010). It can be overcome in the class of 2D Harris-type isotropic equilibria (Schindler, 1972) by applying an external driving electric field to squeeze the CS down to electron scales and to reach the electron tearing instability threshold (Hesse & Schindler, 2001; Pritchett, 2005, 2010; Liu et al., 2014). It can also be overcome for a class of thicker isotropic CS equilibria assuming the ion tearing destabilization if the tail has a region with an accumulated magnetic flux (M. I. Sitnov & Schindler, 2010; M. I. Sitnov et al., 2013, 2014; Bessho & Bhattacharjee, 2014; Pritchett, 2015; M. I. Sitnov et al., 2017). In both scenarios the X-line forms close to the near-Earth boundary of the simulation box ($\sim 15-20d_i$, where d_i is the ion inertial length). Thus, these scenarios leave open the question how such thin CSs can be formed relatively far from the Earth, where the X-lines are usually observed ($\gtrsim 15R_E$, where R_E is the Earth's radius (e.g. Nagai et al., 2005)), in realistic, that is, weakly anisotropic plasmas.

The tearing stability analysis using the self-consistent non-Harris TCS equilibria has been performed in (L. Zelenyi et al., 2008) using an ion distribution with counter-streaming field-aligned flows of warm plasma outside the CS. That study revealed regions of the ion tearing instability for substantial ion anisotropy, when the bulk flow velocity v_D of the counter-streaming flows exceeds their thermal speed v_{Ti}. Whether such unstable regions exist in weakly anisotropic plasmas remained unclear, in particular, because the corresponding equilibrium theory (M. I. Sitnov et al., 2000; L. M. Zelenyi et al., 2004) did not have the Harris limit (M. I. Sitnov et al., 2000). On the other hand, earlier studies (Burkhart et al., 1992a) revealed no new instability regions in the limit of strong ion anisotropy $v_D \gg v_{Ti}$. This controversial picture points to the importance of formulating a tractable description of the multiscale TCS equilibria with weakly anisotropic plasmas assuming the Harris model in the limit of plasma isotropy.

The multiscale CS structure could be explained by the plasma anisotropy (Cowley, 1978; M. I. Sitnov et al., 2000; Schindler & Birn, 2002; M. I. Sitnov et al., 2003; Birn et al., 2004; L. M. Zelenyi et al., 2004), or agyrotropy (M. I. Sitnov et al., 2000, 2003) due to the quasiadiabatic ion motions (Speiser, 1965; Sonnerup, 1971; Büchner & Zelenyi, 1989). However, the electron anisotropy can explain only 10-30% of the observed current density (Artemyev et al., 2016). The field-aligned ion anisotropy could explain the formation of multiscale CSs and their additional elongation due to balancing the magnetic tension by the ion inertia (M. I. Sitnov et al., 2006, and refs. therein). The cor-

responding field-aligned anisotropy has indeed been reported in the tail (Walsh et al., 2011; Artemyev et al., 2019). However, it is relatively weak, so that it remains unclear if it could provide the localization of TCSs on the scale of the thermal ion gyroradius and a substantial current density increase in that region.

In this paper we investigate the limit of weak anisotropy of the TCS model (M. I. Sitnov et al., 2003, hereafter, SGS) whose distinctive feature is its transformation into the Harris model in the limit of zero anisotropy. We show that the weak plasma anisotropy outside TCSs together with plasma agyrotropy inside it can indeed explain many observed properties of embedded TCSs. In particular, 2D weakly anisotropic TCSs have aspect ratios consistent with observations and controlled by the embedding strength.

2 Multiscale current sheet equilibrium

In the kinetic theory, the solution of the system of Vlasov-Maxwell equations for CS equilibria usually starts from the selection of the particle distributions as functions of the corresponding integrals of motion, because it allows one to automatically solve the Vlasov equation. In the original Harris theory (Harris, 1962), the ion and electron distributions were the exponential functions of the total energy $W_\alpha = m_\alpha v^2/2 + q_\alpha \phi$ and the y-component of the canonical momentum $P_{y\alpha} = m_\alpha v_y + (q_\alpha/c)A_y$, where $\alpha = i, e$ is the species index for ions and electrons, ϕ is the electrostatic potential and $\mathbf{A} = (0, A_y(z), 0)$ is the vector potential (initially we discuss a 1-D model, which is independent of x, with the 2-D generalization being addressed further in section 7). In addition, it was assumed that the drift velocities of ions and electrons satisfy the condition $v_{Di}/v_{De} = -T_i/T_e$ to provide the exact neutrality of the resulting solutions with $\phi = 0$.

Two ways to generalize the Harris class of equilibrium CS models have been investigated recently. In the first approach (Schindler & Birn, 2002; Birn et al., 2004) the authors abandoned the assumption of the exponential dependence for the canonical momentum. They also waived the exact neutrality condition to consider electron-dominated TCS. However, with the original set of invariants W_α and $P_{y\alpha}$, the pressure tensor remains isotropic in the plane (v_x, v_z). As a result, $\partial p_{xx}/\partial x = (\partial p/\partial A_y)(\partial A_y/\partial x) = j_y B_z$ and therefore the original isotropic force balance condition is retained (even though the plasma is not isotropic anymore), making such TCSs relatively short.

In another approach, which was first proposed in the SGS model, the set of integrals of motion was extended due to the use of the quasi-adiabatic or sheet invariant (Schindler, 1965; Sonnerup, 1971; Büchner & Zelenyi, 1989)

$$I_z^{(\alpha)} = \frac{1}{2\pi} \oint m_\alpha v_z dz \tag{1}$$

Then the distribution function can be presented in the form

$$f_{0\alpha} \propto \exp\left(\frac{q_\alpha v_{D\alpha}}{cT_{||\alpha}} A_y - \frac{q_\alpha \phi}{T_{||\alpha}}\right) \exp\left\{-\frac{m_\alpha[v_x^2 + (v_y - v_{D\alpha})^2 + v_z^2]}{2T_{||\alpha}}\right\} \times \exp\left[\left(\frac{1}{T_{||\alpha}} - \frac{1}{T_{\perp\alpha}}\right)\frac{\omega_{0\alpha}}{2} I_z^{(\alpha)}\right] \tag{2}$$

where $T_{||\alpha}$ and $T_{\perp\alpha}$ are the parallel and perpendicular temperature parameters, which become true temperatures outside the TCS where plasma is gyrotropic. The drift velocities $v_{D\alpha}$ determine the shift of electron and ion distributions in the y-direction and they determine the CS current in the Harris limit $T_{||\alpha} = T_{\perp\alpha}$; $\omega_{0\alpha}$ is the particle gyrofrequency in the lobe field $B_0 = |B_x(|z| \to \infty)|$. In this paper we investigate the SGS model based on the particle distribution (2) in the limit of weak ion anisotropy ($(T_{||i} - T_{\perp i})/T_{\perp i} \ll 1$) and isotropic electron species ($T_{||e} = T_{\perp e}$).

In the SGS approach, the CS magnetic field as a function of the electromagnetic potential is presented in the form:

$$b(a) = \sqrt{2\beta_0(P_i(a) + P_e(a))} \tag{3}$$

Here $b = B_x/B_0$ is the dimensionless x-component of the magnetic field normalized by its asymptotic value B_0 in the tail lobes. $a = -A_y/(B_0\rho_{\perp 0i})$ is the dimensionless vector-potential and $\rho_{\perp 0i} = v_{T\perp i}/\omega_{0i}$ is the thermal ion gyroradius in the field B_0 based on the perpendicular thermal velocity $v_{T\perp i}$, the temperature parameter $T_{\perp i}$. $\beta_0 = 8\pi n_0 T_{\perp i}/B_0^2$ is the effective plasma beta parameter.

The ion contribution on the right hand side of (3) is determined by the following formula:

$$P_i = \frac{e^{-w_{Di}^2\eta_i(\eta_i-1)}}{\pi}\int_0^a da' e^{(-2\eta_i w_{Di}a' - \eta_i\varphi)}\int w_y dw_y dw_z F(w_y, w_z, a') \tag{4}$$

with the distribution (integrated over v_x) taking the form

$$F = \exp\Big[(\eta_i - 1)I^{(i)} - \eta_i(w_y - w_{Di})^2 - \eta_i w_z^2\Big], \tag{5}$$

and the dimensionless invariant presented as

$$I^{(i)}(a', w_y, w_z) = \frac{2}{\pi}\int_{a_0}^{a_1}\frac{da''}{b(a'')}\sqrt{w_y^2 + w_z^2 + [\varphi(a') - \varphi(a'')] - (w_y + a'' - a')^2} \tag{6}$$

where $a_{0,1} = a' - w_y \mp \sqrt{w_y^2 + w_z^2 + [\varphi(a') - \varphi(a_{0,1})]}$ if $a_0 > 0$ and $a_0 = 0$ if the formal solution for a_0 becomes negative. In these equations $\eta_i = T_{\perp i}/T_{||i}$ is the ion anisotropy parameter, $w_{D\alpha} = v_{D\alpha}/v_{T\perp\alpha}$ are the dimensionless drift velocities of the Harris component of the distribution (2) and $\varphi = e\phi/T_{\perp i}$ is the dimensionless electrostatic potential.

The electron contribution to the right hand side of (3) has the original Harris form of the shifted Maxwellian (and hence isotropic) distribution

$$P_e = -\frac{w_{De}\tau^{1/2}}{\mu^{1/2}}\int_0^a da' e^{2w_{De}\tau^{-1/2}\mu^{-1/2}a' + \tau^{-1}\varphi(a')} \tag{7}$$

where $\tau = T_e/T_{\perp i}$ and $\mu = m_e/m_i$ are electron-to-ion temperature and mass ratios. The dimensionless electrostatic potential is determined by the quasi-neutrality equation:

$$\begin{aligned}\varphi(\tau^{-1} + \eta_i) = \log\{\pi^{-1}\int dw_y dw_z F(w_y, w_z, a)\}\\ -w_{Di}^2\eta_i(\eta_i - 1) - 2a(w_{De}\tau^{-1/2}\mu^{-1/2} + \eta_i w_{Di})\end{aligned} \tag{8}$$

The effective plasma beta parameter β_0 in (3) is the eigenvalue of the system of equations (3), (7) and (8) with the boundary condition $b(\infty) = 1$. The main system of SGS equations is complemented by the condition

$$w_{De} = -w_{Di}\eta_i\tau^{1/2}\mu^{1/2} \tag{9}$$

According to (8), this condition provides the neutrality outside the TCS and transforms into the well known relation $v_{De}/v_{Di} = -T_e/T_i$, which guarantees the neutrality in case

of the Harris solution (e.g. Lembege & Pellat, 1982). In our analysis, based on previous numerical solutions (M. I. Sitnov et al., 2003, 2004, 2006; M. I. Sitnov & Merkin, 2016) it will be used to neglect the charging effects. The latter have been studied in (Panov & Pritchett, 2018; M. I. Sitnov et al., 2021) for the isotropic plasma with shifted Maxwellian distributions and will be further investigated for the SGS model elsewhere.

For completeness, we provide the expression for the plasma density

$$n_i = \frac{n_0}{\pi} e^{-w_{Di}^2 \eta_i(\eta_i-1)} e^{(-2\eta_i w_{Di} a - \eta_i \varphi)} \int dw_y dw_z F(w_y, w_z, a) \tag{10}$$

following from the distribution function adopted in SGS, which we rewrite here in dimensionless variables

$$f_i(z, \mathbf{w}) = \frac{n_0 \eta_i^{1/2}}{\pi^{3/2}} e^{-w_{Di}^2 \eta_i(\eta_i-1)} e^{-2\eta_i w_{Di} a - \eta_i \varphi - \eta_i w_x^2} F(w_y, w_z, a) \tag{11}$$

The constant n_0 in the last two equations is chosen in such a way to yield the Harris profile outside the Harris sheet where $I^i \approx (w_y^2 + w_z^2)$

$$f_i^{(H)}(z, \mathbf{w}) = \frac{n_0 \eta_i^{1/2}}{\pi^{3/2}} e^{-w_{Di}^2 \eta_i(\eta_i-1)} e^{-\eta_i w_x^2 - (w_y - w_{Di})^2 - w_z^2} \tag{12}$$

3 Limit of zero ion anisotropy

In the limit of weak anisotropy $|\eta_i - 1| \ll 1$ we will solve (3), (7) and (8) by iterations. In the zero approximation $\eta_i = 1$, according to (9) and (8), the TCS becomes neutral: $\varphi = 0$. Then (7) yields

$$\begin{aligned} P_e^{(0)} \quad &\approx -\tau^{1/2} \mu^{-1/2} w_{De} \textstyle\int_0^a da' \exp\left(2 w_{De} \tau^{-1/2} \mu^{-1/2} a'\right) \\ &= (\tau/2)\left(1 - e^{2 w_{De} \tau^{-1/2} \mu^{-1/2} a}\right) \approx (\tau/2)\left(1 - e^{-2 w_{Di} a}\right) \end{aligned} \tag{13}$$

while (3) can be reduced to the expression

$$P_i^{(0)} \approx w_{Di} \int_0^a da' \exp\left(-2 w_{Di} a'\right) = (1/2)\left(1 - e^{-2 w_{Di} a}\right) \tag{14}$$

with the same spatial profile as (13) due to the CS neutrality. After substitution of (13) and (14) into (3) we reproduce the original Harris solution in the form

$$b^{(0)}(a) = \sqrt{\beta_0^{(0)}(1+\tau)\left(1 - e^{-2 w_{Di} a}\right)} \tag{15}$$

and then, taking the limit $a = \infty$, we obtain the corresponding eigenvalue (e.g. M. I. Sitnov et al., 2003)

$$\beta_0^{(0)}(1+\tau) = 1 \tag{16}$$

The corresponding eigenfunction, the solution of (15) can be found then by integrating the equation

$$d\zeta = \frac{da}{b^{(0)}(a)} = \frac{da}{\sqrt{1 - e^{-2 w_{Di} a}}} \tag{17}$$

to yield the following formulae of the 1-D Harris model (Harris, 1962; Lembege & Pellat, 1982) presented here in the dimensionless form:

$$\zeta = \log\left(e^{w_{Di}a} + \sqrt{e^{2w_{Di}a} - 1}\right)/w_{Di} \tag{18}$$

$$a^{(0)}(\zeta) = \log\left(\cosh(\zeta w_{Di})\right)/w_{Di} \tag{19}$$

$$b^{(0)}(\zeta) = \tanh\left(\zeta w_{Di}\right) \tag{20}$$

$$j^{(0)}(\zeta) = db^{(0)}/d\zeta = w_{Di}\cosh^{-2}\left(\zeta w_{Di}\right) \tag{21}$$

$$n^{(0)}(\zeta) = n_0\exp\left(-2aw_{Di}\right) = n_0\cosh^{-2}\left(\zeta w_{Di}\right) \propto j(\zeta), \tag{22}$$

where $\zeta = z/\rho_{\perp 0i}$ and $a = \int_0^\zeta b(\zeta')d\zeta'$, suggests that the CS thickness $L = \rho_{0i}/w_{Di}$ (where we omit the index $\perp$ because of the isotropic plasma limit).

4 Approximation of weak plasma anisotropy and strong embedding

To guide the subsequent analytic approximations, we first survey numerical solutions of the system of equilibrium equations (3)-(8) in the region of weak ion anisotropy characterized by the small parameter $|\delta_1| \ll 1$, where $\delta_1 = 1 - \eta_i$. We further focus on the subregion of the strong embedding characterized by another small parameter $\delta_2 = w_{Di} \ll 1$ (note that in case of $\delta_1 < 0$ it may also be the limit of strong CS bifurcation, which is not studied below). We indeed expect strong TCS embedding/bifurcation in the limit $\delta_2 \ll 1$, because the Speiser orbit size in this limit is much smaller than the Harris CS half-thickness L_H (20): $L_{TCS} \sim \rho_{0i} \ll \rho_{0i}/\delta_2 = L_H$.

The corresponding profiles of the magnetic field, plasma and current density, electrostatic potential and the local ion temperature anisotropy for $\delta_2 = 0.125$ and the anisotropy values $\delta_1 = 0.05{-}0.4$ as functions of the dimensionless potential a and the coordinate ζ are presented, respectively, in Figs. 1 and 2. These figures confirm our Speiser-orbit hypothesis: Figs. 1c and 2c show that the TCS current density is largely changing in the region $a \lesssim 1$ (or $\zeta \lesssim 1$). The corresponding changes of the plasma density (Figs. 1b and 2b) as well as the dimensionless electrostatic potential (Figs. 1d and 2d) are relatively small. The resulting changes of the magnetic field profile (Figs. 1a and 2a) are largely limited to the Speiser-orbit area $a \sim 1$.

The first-order (in the anisotropy strength δ_1) modification of the isotropic solution (15) can be presented using (3) as follows

$$b^{(0)} + b^{(1)} = \sqrt{2\left(\beta_0^{(0)} + \beta_0^{(1)}\right)\left(P_i^{(0)} + P_i^{(1)} + P_e^{(0)} + P_e^{(1)}\right)} \tag{23}$$

where, according to (15) with the distribution function F (5) expanded into a Tailor series in δ_1,

$$P_i^{(0)} + P_i^{(1)} \approx P_{iA}^{(1)} + P_{iS}^{(1)} \equiv \frac{1}{2}\left(1 - e^{-2\delta_2(1-\delta_1)a}\right)$$
$$-\frac{\delta_1}{\pi}\int_0^a da' e^{-2\delta_2(1-\delta_1)a'}\int w_y dw_y dw_z\left(I^{(i)} - w_y^2 - w_z^2\right)e^{(-w_y^2-w_z^2)} \tag{24}$$

and according to (7), (9) and (13),

$$P_e^{(0)} + P_e^{(1)} \approx \frac{\tau}{2}\left(1 - e^{-2\delta_2(1-\delta_1)a}\right) \tag{25}$$

Note that neither in (24) nor in (25) the expression $\exp\left(-2\delta_2(1-\delta_1)a\right)$ can be expanded into a series in δ_1 because its exponent scales as $\propto a$ and therefore it can be substantial even for small values of δ_1 and δ_2 outside of the TCS where $a \to \infty$. Note also that

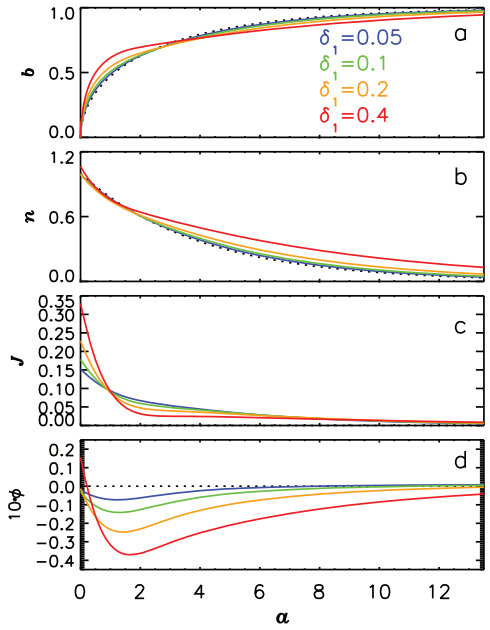

Figure 1. The profiles of (a) the dimensionless magnetic field b, (b) plasma density n, (c) current density j and (d) electrostatic potential φ as functions of the dimensionless vector-potential a for different values of the ion anisotropy parameters $1 - \eta_i \equiv \delta_1 = 0.05, 0.1, 0.2$, and 0.4 (dotted black lines show the zero anisotropy limit solutions). Other parameters in the system of equilibrium equations (3)-(8) are as follows: $\eta_e = 1$, $\mu = 1/16$, $\tau = 1/4$, $w_{Di} \equiv \delta_2 = 0.125$.

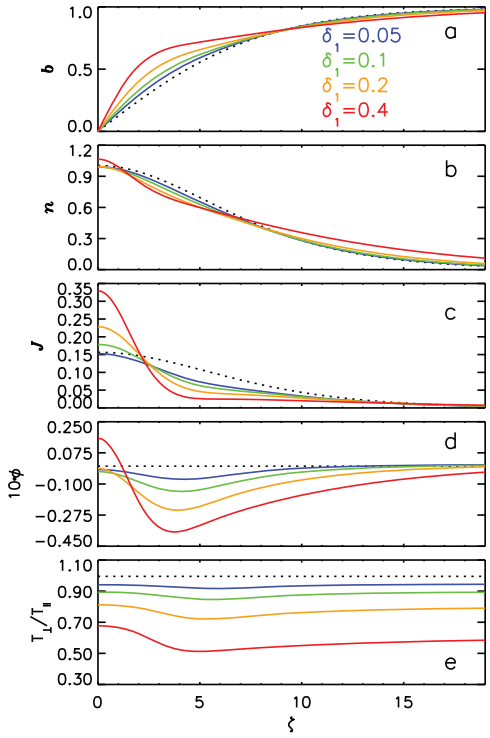

Figure 2. The profiles similar to those in Fig. 1 but now as functions of the dimensionless coordinate $\zeta = z/\rho_{\perp 0i}$. The additional panel (e) shows the profiles of the local ion temperature anisotropy $\eta_i = T_{\perp i}/T_{||i}$.

we split the corrected ion contribution to the pressure-type term $P_i^{(0)} + P_i^{(1)}$ into two parts $P_{iA}^{(1)}$ and $P_{iS}^{(1)}$ to separate corrections due to the Harris velocity shift (as well as the ion anisotropy) and the contribution provided by quasi-adiabatic Speiser orbits (the ion agyrotropy). We also neglected the electrostatic potential φ in view of (9) and Figure 1d.

Since the last two terms in the penultimate bracket of $P_{iS}^{(1)}$ in (24) disappear due to the factor w_y in the integrand it can be re-written as follows:

$$P_{iS}^{(1)} = -\delta_1 \pi^{-1} \int_0^a da' \exp\left(-2\delta_2(1-\delta_1)a'\right) \int w_y dw_y dw_z I^{(i)} \exp\left(-w^2\right) \tag{26}$$

where $w^2 = w_y^2 + w_z^2$ and $I^{(i)}$ is determined by (6) with $b(a) = b^{(0)}(a) = \sqrt{1 - e^{-2\delta_2 a}}$ and

$$I^{(i)}(a', w_y, w_z) = \frac{2}{\pi} \int_{a_0}^{a_1} \frac{da''}{\sqrt{1 - e^{-2\delta_2 a''}}} \sqrt{w_y^2 + w_z^2 - (w_y + a'' - a')^2} \tag{27}$$

The latter formula can also be simplified, taking into account that the asymmetry of $I^{(i)}$ in the velocity space is limited by the TCS vicinity ($a \sim 1$; see the details of the distribution function below), where $\delta_2 a \ll 1$ and therefore, according to (15), $b^{(0)} \approx \sqrt{2\delta_2 a}$. Hence the quasi-adiabatic invariant $I(z)$ can be simplified as follows

$$I^{(i)}(a', w_y, w_z) \approx \frac{2}{\pi\sqrt{2\delta_2}} \int_{a_0}^{a_1} \frac{da''}{\sqrt{a''}} \sqrt{w^2 - (w_y + a'' - a')^2} \tag{28}$$

The integral (28) describes the quasi-adiabatic invariant in the simplified magnetic field $B_x \propto x$, which was investigated before in (Sonnerup, 1971; Büchner & Zelenyi, 1989; L. M. Zelenyi et al., 1990).

It is important to note here that the main integral over a' in (26) cannot be simplified similar to (28) because of a very slow convergence of the rest of the integrand as is shown below. Instead of that we present (26) in the form

$$P_{iS}^{(1)} = \frac{2\delta_1}{\pi^2\sqrt{2\delta_2}} b^{(tcs)}(a, \delta_2(1-\delta_1)) \tag{29}$$

where

$$b^{(tcs)}(a, \delta) = \int_0^a da' j^{(tcs)}(a') e^{-2\delta a'} \tag{30}$$

and

$$j^{(tcs)}(a') = -\int w_y e^{-w^2} dw_y dw_z \int_{a_0}^{a_1} \frac{da''}{\sqrt{a''}} \sqrt{w^2 - (w_y + a'' - a')^2} \tag{31}$$

Let us consider the limiting cases for function $j^{(tcs)}(a')$. In the limit $a' \to 0$, the lower limit of the second integral in (31) $a_0 \to 0$ and hence after the substitution $x = a'' + w_y - a'$

$$j^{(tcs)}(a' \to 0) = -\int w_y e^{-w^2} dw_y dw_z \int_{w_y}^{w} \frac{dx\sqrt{w^2 - x^2}}{\sqrt{x - w_y}} = j_{(0)}^{(tcs)} \approx 1.77 \tag{32}$$

In another limit $a' \to \infty$,

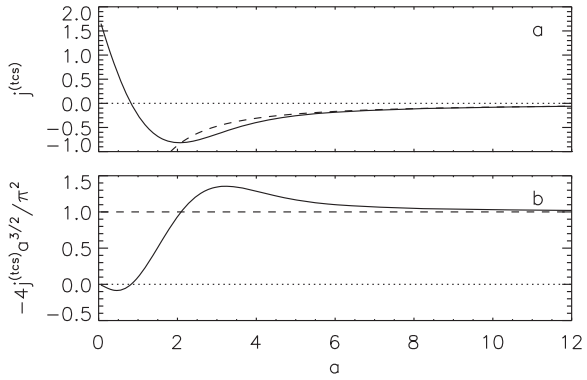

Figure 3. (a) The profile of the dimensionless TCS current correction $j^{(tcs)}(a)$ to the isotropic solution given by the formula (31) and (b) its comparison with the asymptotic approximation (34) in the limit $a \to \infty$. The latter is also shown in panel (a) by the dashed line. Dotted lines show zero levels of $j^{(tcs)} = 0$ and $-4j^{(tcs)}a^{3/2}\pi^{-2}$, while the dashed line in panel (b) shows the level $-4j^{(tcs)}a^{3/2}\pi^{-2} = 1$.

$$\begin{aligned} j^{(tcs)}(a') &\approx -\int w_y e^{-w^2} dw_y dw_z \int_{-w}^{w} \frac{dx\sqrt{w^2-x^2}}{\sqrt{x+a'-w_y'}} \\ &\approx -\frac{1}{2(a')^{3/2}} \int w_y^2 e^{-w^2} dw_y dw_z \int_{-w}^{w} dx\sqrt{w^2-x^2} \end{aligned} \tag{33}$$

To simplify the integral above, we expanded the expression $1/\sqrt{x+a'-w_y'} \approx 1/\sqrt{a'} + (w_y - x)(a')^{-3/2}/2$ and took into account that its first and last terms make zero contributions for symmetry considerations. Calculating the error integrals in (33), we obtain eventually

$$j^{(tcs)}(a)_{|a'\to\infty} \approx -(\pi^2/4)a^{-3/2} \tag{34}$$

The full profile of the dimensionless TCS current-like parameter $j^{(tcs)}(a)$ as well as its comparison with the asymptotic formula (34) are provided in Figure 3.

Now, the electric current with TCS corrections can be written as db^2/da or

$$\begin{aligned} j^{(0)}(a) + j^{(1)}(a) &= \frac{1}{2}\frac{db^2}{da} \\ &= \left(\beta_0^{(0)} + \beta_0^{(1)}\right) \frac{d}{da}\left(P_e + P_i^{(0)} + P_i^{(1)}\right) \\ &= \left(\frac{1}{1+\tau} + \beta_0^{(1)}\right)\left(\delta_2(1-\delta_1)(1+\tau)e^{-2\delta_2(1-\delta_1)a} + \frac{dP_{iS}^{(1)}}{da}\right) \\ &= \delta_2 e^{-2\delta_2(1-\delta_1)a}\left(\frac{1}{1+\tau} + \beta_0^{(1)}\right)\left((1-\delta_1)(1+\tau) + \frac{2\delta_1 j^{(tcs)}(a)}{\pi^2\delta_2\sqrt{2\delta_2}}\right) \end{aligned} \tag{35}$$

Here the corrections to the eigenvalue of the equilibrium solution from (24) $\beta_0^{(1)}$ is found from the equation

$$\left(\beta_0^{(0)} + \beta_0^{(1)}\right)\left(1 + \tau + \frac{4\delta_1 b^{(tcs)}(\infty, \delta_2(1-\delta_1))}{\pi^2\sqrt{2\delta_2}}\right) = 1 \tag{36}$$

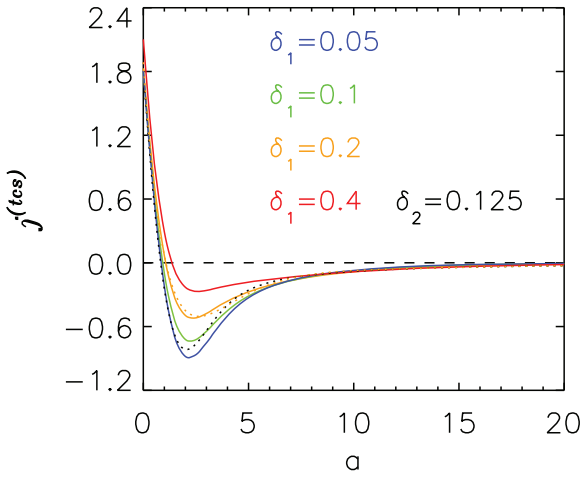

Figure 4. (a) The comparison of the universal function $j^{(tcs)}$ (31) (black dotted line), which is also shown in Figure 3, with similar $j^{(tcs)}$ derived from the numerical solutions for the current density shown in Figure 1c using its presentation in the form (35) for $\delta_2 = 0.125$ and different values of the anisotropy parameter δ_1. The yellow dotted line shows the analytical approximation (37)-(38) of the derived function $j^{(tcs)}_{\delta_1=0.2}$ (solid yellow line).

The presentation of the current density in the form (35) can be used to compare the universal function $j^{(tcs)}$ (31) with the numerical solutions shown in Figure 1c. The comparison results are presented in Figure 4. They show that while in the limits $a \to 0$ and $a \to \infty$ all exact numerical solutions are indeed close to the universal profile (31) this is not the case for $a \sim 2.5$. Therefore, to avoid strong deviations from the range of the parameter δ_1 considered here we generated a trade-off by using an analytical representation of $j^{(tcs)}$ based on its numerical analog for $\delta_1 = 0.2$ (yellow solid line in Figure 4)

$$j^{(tcs)} \approx (a_{[0]} - a_{[1]}a)e^{-a_{[2]}a} + h(a) \tag{37}$$

where $\mathbf{a} = (1.88711, 1.75717, 0.646603)$ and the function

$$h(a) = -(\pi^2/4)(1 - e^{-(a/a_h)^{7/2}})a^{-3/2} \tag{38}$$

takes into account the non-exponential "halo" decay of $j^{(tcs)}$ reflected by (34) and important only for sufficiently large values of a, so that $a_h = 10$. The approximation (37)-(38) is shown in Figure 4 by the yellow dotted line.

The comparison of the numerical profiles of the current density similar to those in Figure 1c (but here not normalized by β_0) with their approximations based on the presentation (35) with the analytical approximation (37)-(38) for $j^{(tcs)}$ is shown in Figure 5.

The presentation of the universal current density correction $j^{(tcs)}$ in the form (37)-(38) allows one to present the resulting magnetic field $b(a) = \sqrt{2\int_0^a j(a')da'}$ (see also (23)) in the form

$$b^{(0)} + b^{(1)} = \sqrt{\left(\beta_0^{(0)} + \beta_0^{(1)}\right)\left((1+\tau)\left(1 - e^{-2\delta_2(1-\delta_1)a}\right) + 2P_{iS}^{(1)}\right)} \tag{39}$$

with $P_{iS}^{(1)}$ given by (29) and

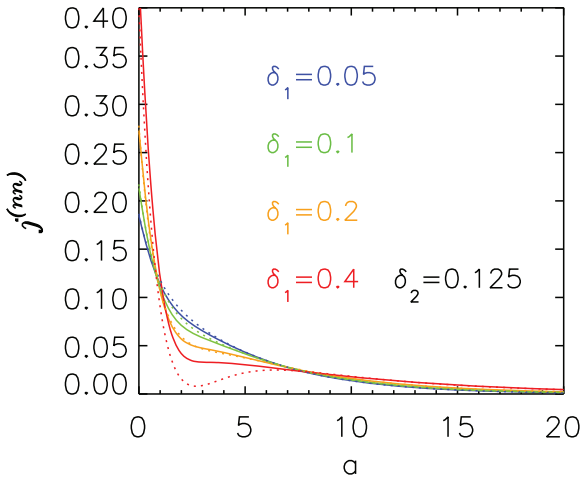

Figure 5. The profiles of the current density $j^{(nn)}$ similar to those shown in Figure 1c but here not normalized by β_0 (solid lines), compared to similar profiles obtained from the approximation (35) for the current density and the analytical approximation (37)-(38) for the universal function $j^{(tcs)}$ (31).

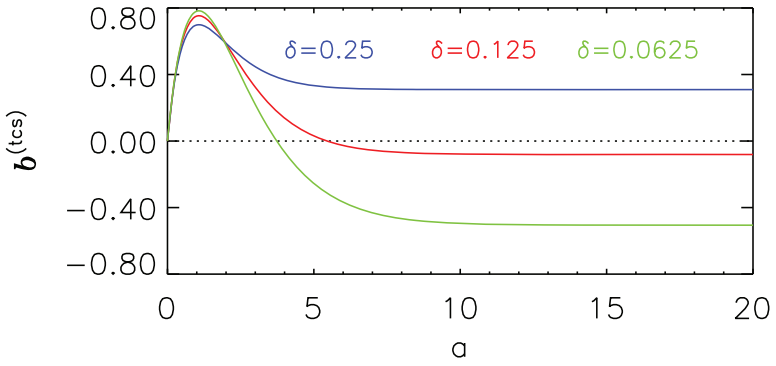

Figure 6. The magnetic field correction function $b^{(tcs)}(a, \delta)$ for different values of the parameter $\delta = 0.25$, 0.125 and 0.0625.

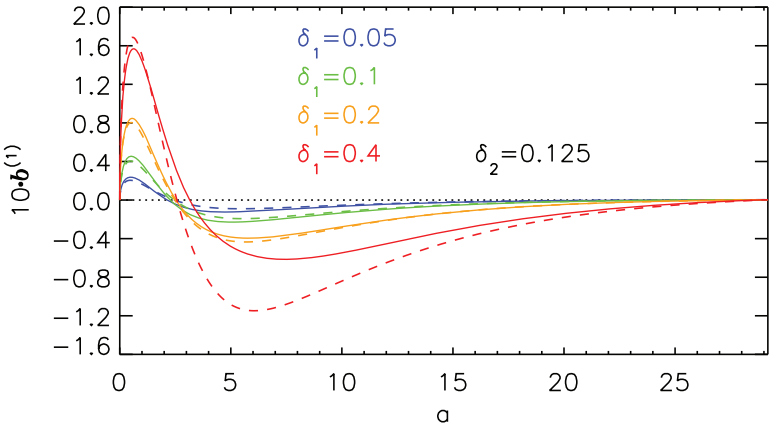

Figure 7. TCS correction to the magnetic field $b^{(1)}(a)$ (solid lines) and it approximations corresponding to formulae (39) and (40) (dashed lines) for different values of the parameter $\delta_1 = 0.05 - 0.4$ and $\delta_2 = 0.125$.

$$b^{(tcs)}(a,\delta) \approx \left[\frac{a_{[0]}}{2\delta + a_{[2]}} - \frac{a_{[1]}}{(2\delta + a_{[2]})^2}\right]\left[1 - e^{-(2\delta + a_{[2]})a}\right] + \frac{a_{[1]}a}{2\delta + a_{[2]}} e^{-(2\delta + a_{[2]})a} \tag{40}$$

The latter approximate formula was obtained by the integration of (37) according to (30) and neglecting the halo term (38) whose contribution is reduced in (30) by the factor $e^{-2\delta_2(1-\delta_1)a'}$. The function $b^{(tcs)}(a,\delta)$ is presented for several different values of δ in Figure 6.

It is convenient to present the resulting magnetic field (39) in the form

$$b^{(0)} + b^{(1)} \approx \sqrt{1 - e^{-2\delta_2' a} + \frac{4\delta_1 b^{(tcs)}(a,\delta_2')}{\pi^2(1+\tau)\sqrt{2\delta_2}}} \Big/ \sqrt{1 + \frac{4\delta_1 b^{(tcs)}(\infty,\delta_2')}{\pi^2(1+\tau)\sqrt{2\delta_2}}} \tag{41}$$

(with $\delta_2' = \delta_2(1-\delta_1)$), which helps one to compare the new expression for the magnetic field in weakly anisotropic TCSs with the Harris formula (15). It is also useful for further analysis.

The numerical solutions of the original SGS model (3)-(7) with the ion to electron drift velocity ratio (8) similar to the Harris model are compared in Figure 7 with the new analytical approximations (40)-(41) in the form of the difference $b^{(1)}$ from the corresponding Harris solutions $b^{(0)}$. This comparison confirms a reasonable accuracy of these analytical approximations in the double limit of weak anisotropy ($\delta_1 \ll 1$) and strong embedding ($\delta_2 \ll 1$). Note that the use of δ_2 instead of δ_2' in (41) would result in missing the characteristic valley in function $b^{(1)}(a)$ outside of the TCS ($a \gtrsim 3$).

Finally, according to (10), the correction to the plasma density can be presented in the form similar to (24)

$$n^{(1)} + n^{(0)} \approx n_0 e^{-2\delta_2' a} + n_{iS}^{(1)}, \tag{42}$$

where

$$n_{iS}^{(1)} = -\frac{\delta_1 n_0}{\pi} e^{-2\delta_2' a} \int dw_y dw_z \left(I^{(i)} - w_y^2 - w_z^2\right) e^{-w_y^2 - w_z^2} \tag{43}$$

and $I^{(i)}$ is given by (6).

Note that we cannot simplify here the magnetic field profile by $b^{(0)} \approx \sqrt{2\delta_2 a''}$ as we did for current density in (28). However, since outside the neutral plane where $b(a)$ changes slowly, $I^{(i)}$ can be approximated there as the magnetic moment for adiabatic motions $I^{(i)}(a, w_y, w_z) \approx (w_y^2 + w_z^2)/b(a)$ to yield

$$n_{iS}^{(1)} \approx \delta_1 n_0 e^{-2\delta_2' a} \left(1 - (b^{(0)}(a))^{-1}\right) \approx -(1/2)\delta_1 n_0 e^{-2(\delta_2' + \delta_2)a} \tag{44}$$

In another limit $\delta_2 a \ll 1$ one can still use the approximation $b^{(0)} \approx \sqrt{2\delta_2 a''}$ in (43) to get

$$I^{(i)}(a, w_y, w_z) = \frac{2}{\pi\sqrt{2\delta_2}} \int_{a_0}^{a_1} \frac{da''}{a''} \sqrt{w_y^2 + w_z^2 - (w_y + a'' - a)^2} \tag{45}$$

which can be simplified in the limit $a \to 0$ similar to (32) by making the lower limit of the integral in (45) $a_0 \to 0$ and hence after the substitution $x = a'' + w_y - a$ it transforms into

$$I^{(i)}(a, w_y, w_z) = \frac{2}{\pi\sqrt{2\delta_2}} \int_{w_y}^{w} \frac{dx\sqrt{w^2 - x^2}}{\sqrt{x - w_y}} \tag{46}$$

to yield eventually for the TCS density correction

$$\begin{aligned} n_{iS}^{(1)} = -\frac{\delta_1 n_0}{\pi} e^{-2\delta_2 a} \int dw_y dw_z \left(\frac{2}{\pi\sqrt{2\delta_2}} \int_{w_y}^{w} \frac{dx\sqrt{w^2 - x^2}}{\sqrt{x - w_y}} - w_y^2 - w_z^2 \right) e^{-w_y^2 - w_z^2} \\ = -n^{(0)}\delta_1 \left(O\left(\frac{1}{\sqrt{\delta_2}}\right) + O(1) \right) \end{aligned} \tag{47}$$

One can refrain from a more detailed numerical evaluation of (47), because the estimates of the current density correction made in the next section show that the relative perturbation of the plasma density is smaller than the corresponding relative perturbation of the current density by the factor $\delta_2 \ll 1$. Thus, in the leading approximation, the plasma density perturbation is determined by the first term in right hand side of (42), which is consistent with the original numerical results provided in Figure 1b.

5 TCS correction in real space

The real-space solution with the TCS correction can now be obtained from the definition of $b(a)$

$$d\zeta = \frac{da}{b^{(0)}(a) + b^{(1)}(a)} \tag{48}$$

or with the expansion of (41) in a series of $O(b^{(tcs)})$,

$$d\zeta = \frac{da}{\sqrt{1 - e^{-2\delta_2' a}}} \left[1 - \frac{2\delta_1}{(1+\tau)\pi^2\sqrt{2\delta_2}} \left(\frac{b^{(tcs)}(a, \delta_2')}{1 - e^{-2\delta_2' a}} - b^{(tcs)}(\infty, \delta_2') \right) \right] \tag{49}$$

Since we solve the problem by iterations, the solution of (49) can be presented in the form

$$a(\zeta) \equiv a_1(\zeta) = \log\left(\cosh(\zeta_1(\zeta)\delta_2')\right)/\delta_2' \tag{50}$$

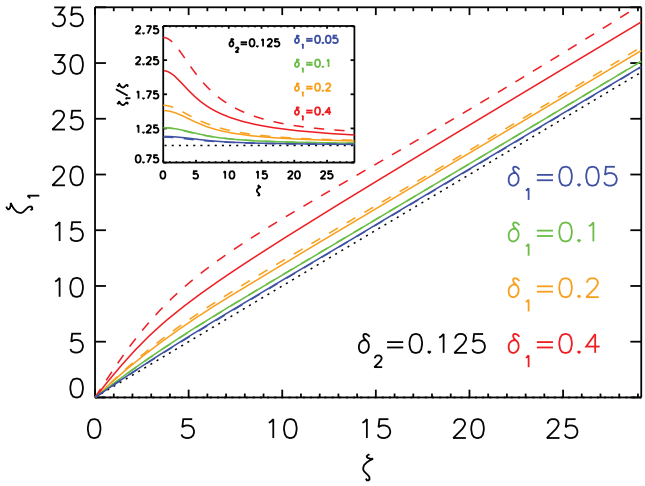

Figure 8. The function $\zeta_1(\zeta)$ (solid lines) and its approximation (54)-(55) (dashed lines) for $\delta_2 = 0.125$ and different values of the parameter $\delta_1 = 0.05, 0.1, 0.2$ and 0.4. The Inset shows the corresponding ratio ζ_1/ζ.

where

$$\zeta_1(\zeta) = \int_0^\zeta d\zeta' \left[1 + \frac{2\delta_1}{(1+\tau)\pi^2\sqrt{2\delta_2}}\left(\frac{b^{(tcs)}(a_0(\zeta'),\delta_2')}{1-e^{-2\delta_2' a_0(\zeta')}} - b^{(tcs)}(\infty,\delta_2')\right)\right]$$
$$= \zeta\left[1 + \frac{2\delta_1}{(1+\tau)\pi^2\sqrt{2\delta_2}}\Delta\zeta(\zeta,\delta_2')\right] \tag{51}$$

and

$$\Delta\zeta(\zeta,\delta_2') = \frac{1}{\zeta}\int_0^\zeta d\zeta'\left(\frac{b^{(tcs)}(a_0(\zeta'),\delta_2')}{1-e^{-2\delta_2' a_0(\zeta')}} - b^{(tcs)}(\infty,\delta_2')\right) \tag{52}$$

and $a_0(\zeta)$ is determined by the same isotropic solution (19): $a_0(\zeta) = \log(\cosh(\zeta\delta_2))/\delta_2$.

In the limit $\zeta \to 0$ the function $\Delta\zeta(\zeta,\delta_2')$ can be evaluated as

$$\Delta\zeta(\zeta,\delta_2')_{|\zeta\to 0} = j_{(0)}^{(tcs)}(2\delta_2')^{-1} - b^{(tcs)}(\infty,\delta_2') \tag{53}$$

where $j_{(0)}^{(tcs)}$ and $b^{(tcs)}(\infty,\delta_2)$ are determined by (32) and (40).

In the opposite limit $\zeta \to \infty$, since the integral in (52) converges to a constant value, the function $\Delta\zeta$ can be estimated as $O(1/\zeta)$. This allows us to approximate the function $\zeta_1(\zeta)/\zeta$ as follows:

$$\frac{\zeta_1(\zeta)}{\zeta} \approx 1 + \frac{\delta_1(j_{(0)}^{(tcs)} - 2\delta_2' b^{(tcs)}(\infty,\delta_2'))}{(1+\tau)\pi^2\delta_2'\sqrt{2\delta_2}}\zeta^{(tcs)}(\zeta) \tag{54}$$

where

$$\zeta^{(tcs)}(\zeta) = z_{[0]}\cosh^{-2}(z_{[1]}\zeta) + (1-z_{[0]})(1+z_{[2]}\zeta^2)^{-1/2} \tag{55}$$

where $\mathbf{z} = (-0.123147, 0.033777, 0.0423979)$.

Numerical profiles of the function ζ_1/ζ are presented in Figures 8 and 9. Figure 8 shows a reasonable consistency with the analytical approximation (54)-(55). It also confirms the corresponding scaling of the parameter $(\zeta_1 - \zeta)/\zeta \propto \delta_1$. According to Figure 9, another analytical scaling suggested by (54), $(\zeta_1 - \zeta)/\zeta \propto {\delta_2}^{-3/2}$, is more limited (see, in particular, the blue lines in Figure 9 corresponding to $\delta_2 = 0.0625$). This

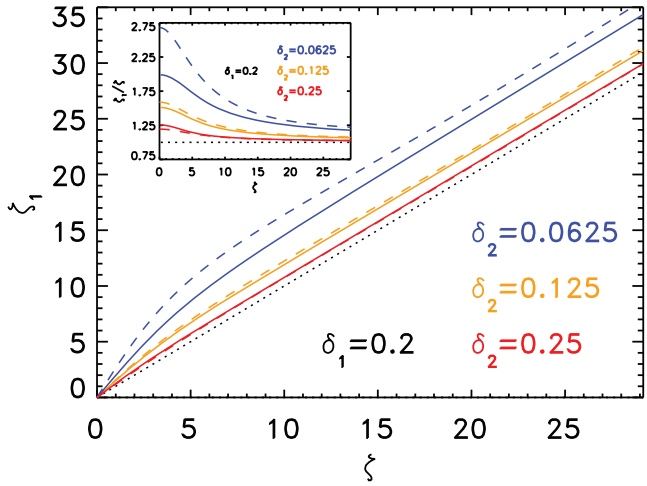

Figure 9. The function $\zeta_1(\zeta)$ (solid lines) and its approximation (54)-(55) (dashed lines) for $\delta_1 = 0.2$ and different values of the parameter $\delta_2 = 0.0625, 0.125$ and 0.25. The Inset shows the corresponding ratio ζ_1/ζ.

is because the approximation of the strong embedding is singular and the resulting correction rapidly increases with the decrease of the embedding parameter δ_2, and it may become controversial even when $\delta_1 \ll 1$, especially when $\delta_2 < \delta_1$. Note that just like for $j^{(tcs)}(a)$ in (37), the fit of $\zeta^{(tcs)}(\zeta)$ in (55) was made using the numerical solution of the original SGS model with the parameters $\delta_1 = 0.2$ and $\delta_2 = 0.125$. There we neglected the possible dependence of δ_2, which can be surmised from (52), because of its asymptotic $\zeta_1(\zeta)/\zeta_{|\zeta\to\infty} = O(1/\zeta)$ and the limited region of ζ_2 values when the combined approximation of small anisotropy and strong embedding is valid.

In summary, according to (41) and (49), the expression for the magnetic field in the real space takes the form

$$b(\zeta,\delta_1,\delta_2) = \sqrt{\tanh^2\left(\delta_2'\zeta_1(\zeta)\right) + \frac{4\delta_1 b^{(tcs)}(a^{(0)}(\zeta),\delta_2')}{\pi^2(1+\tau)\sqrt{2\delta_2}}} \Big/ \sqrt{1 + \frac{4\delta_1 b^{(tcs)}(\infty,\delta_2')}{\pi^2(1+\tau)\sqrt{2\delta_2}}}. \tag{56}$$

where the functions ζ_1, $b^{(tcs)}$ and $a^{(0)}$ are defined by (54)-(55), (40) and (19).

Finally, the electric current with TCS corrections can be written as $(1/2)db^2/da$ and according to (36), we have

$$j^{(0)}(\zeta) + j^{(1)}(\zeta) = \left[\frac{\delta_2'}{\cosh^2\left(\zeta_1\delta_2'\right)} + \frac{2\delta_1 j^{(tcs)}(a^{(0)}(\zeta))}{(1+\tau)\pi^2\sqrt{2\delta_2}\cosh^2\left(\zeta\delta_2'\right)}\right]\left(1 + \frac{4\delta_1 b^{(tcs)}(\infty,\delta_2')}{(1+\tau)\pi^2\sqrt{2\delta_2}}\right)^{-1} \tag{57}$$

As one can see from this expression, the ratio $j^{(1)}/j^{(0)}$ scales as $\delta_1\delta_2^{-3/2}$, which is by the factor $1/\delta_2'$ larger compared to the corresponding relative value of the density correction (42)-(47). Thus, consistent with Figures 1 and 2, the current density perturbation (57) is the main correction in the weakly anisotropic TCS theory within the framework of the SGS model.

6 Ion distribution function

According to (2) and the new notations of the weakly anisotropic TCS theory, the ion distribution can be written in the form

$$f_{0\alpha}(a,\mathbf{w}) \propto \exp\left(-2_i\delta_2' a - \eta_i\varphi\right) \exp\left\{-\delta_1 I^{(i)} - \eta_i[w_x^2 + (w_y-\delta_2)^2 + w_z^2]\right\} \quad (58)$$

Let us simplify now the expression for the sheet invariant I_z. Using the transformation $x = a''/w$, the approximate expression for the quasiadiabatic invariant (28) can be rewritten as

$$I^{(i)}(a,w_y,w_z) \approx \frac{2w^{3/2}}{\pi\sqrt{2\delta_2}} I_S\left(\frac{a-w_y}{w}\right) \quad (59)$$

where

$$I_S(\xi) = \int_{x_0}^{x_1} \frac{dx}{\sqrt{x}}\sqrt{1-(x-\xi)^2} \quad (60)$$

is the integral over quasi-adiabatic (Speiser) orbits, with the condition $x_{0,1} = \xi \mp 1$ if $\xi > 1$ and $x_0 = 0$ if $\xi < 1$, which describes orbits not crossing the neutral plane = 0 and crossing it (figure-of-eight orbits), respectively. It was introduced by Schindler (1965) and further investigated by Sonnerup (1971).

Since $a > 0$, the argument of I_S in (59) is limited by the interval $(-1,\infty)$. Therefore, one can consider the function I_S in two intervals:

1) $|\xi| < 1$.

$$I_S(\xi) = \frac{4\sqrt{2}}{3}\left[(1-k^2)K(k) + (2k^2-1)E(k)\right] \equiv \frac{4\sqrt{2}}{3} f_A(k) \quad (61)$$

where $k = \sqrt{(1+\xi)/2}$. The function $f_A(k)$ was introduced in (Büchner & Zelenyi, 1989) following (Sonnerup, 1971).

2) $\xi > 1$

$$I_S(\xi) = \frac{4\sqrt{2}}{3}\left[2k(1-k^2)K(1/k) + k(2k^2-1)E(1/k)\right] \equiv \frac{4\sqrt{2}}{3} f_B(k) \quad (62)$$

where f_B is another function introduced in (Büchner & Zelenyi, 1989)It is important to note here that the definitions of elliptic integrals in (61)-(62) are different from some textbooks (e.g. Abramowitz & Stegun, 1964): $K, E(m)_{S1971} = K, E(m^2)_{AS1964}$. However, they are consistent with the most recent definitions provided by the Digital Library of Mathematical Functions (DLMF, n.d.).

The profile (60) for $I_S(\xi)$ is also relatively easy to calculate numerically, as well as to obtain the corresponding asymptotics. In particular, for $\xi \to 1+0$

$$I_S(\xi) \approx \frac{\pi}{\sqrt{2}}(1+\xi), \quad (63)$$

while in the limit $\xi \to \infty$.

$$I_S(\xi) \approx \frac{\pi}{2}\frac{1}{\sqrt{\xi}}, \quad (64)$$

The profile of the Schindler-Sonnerup invariant $I_S(\xi)$ given by (60), its asymptotics (63) and (64), as well as approximations by elliptic integrals K, E are presented in Figure 10. The corresponding sample distributions showing paramagnetic and diamagnetic

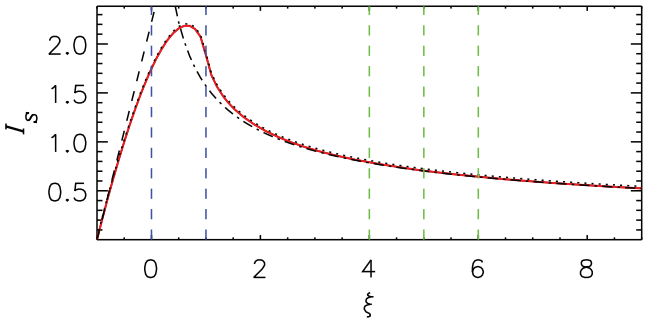

Figure 10. The profile $I_S(\xi)$ given by (60) and drawn with a red line. Its asymptotics (63) and (64) are drawn with dashed and dash-dotted lines, respectively, whereas its approximation by complete elliptic integrals (shifted by 0.02) is drawn with a dotted line. Vertical blue dashed lines on the left together with the ordinate axis mark the region $-1 < \xi < 1$, which describes variability of the parameter $\xi = (a - w_y)/w$ at the TCS center ($a = 0$) and is discussed in the text. Vertical green dashed lines on the right show similar regions of positive and negative w_y variations around another value of the vector-potential $a = 5$, sampled outside the TCS.

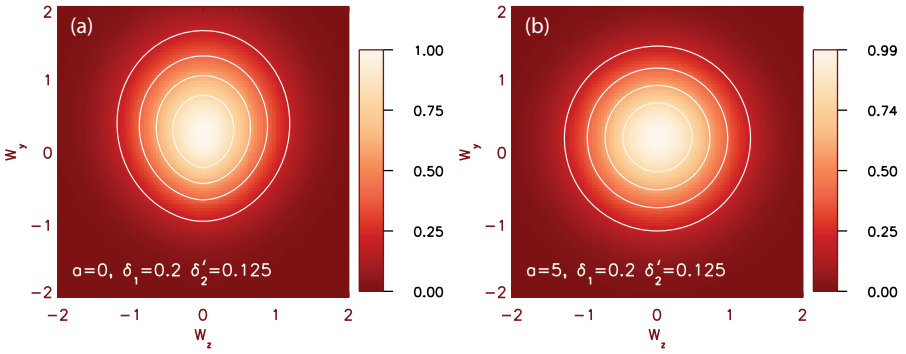

Figure 11. Sample ion distributions (a) at the TCS center ($a = 0$) and (b) at its edge ($a = 5$) for the parameters $\delta_1 = 0.2$ and $\delta_2' = 0.125$.

features of the TCS at its center ($a = 0$) and at the edges ($a = 5$) are presented in Figure 11. Two blue dashed vertical lines in Figure 10 together with the ordinate axis mark the region $-1 < \xi < 1$, which describes variability of the parameter $\xi = (a - w_y)/w$ at the TCS center ($a = 0$). Different values of the parameter I_S within this region for positive and negative values of w_y explain the distribution asymmetry demonstrated in Figure 11a with its larger values for $w_y > 0$. The opposite (diamagnetic) effect outside the TCS is illustrated in Figure 11b with the set of three green dashed vertical lines in Figure 10, which predict a negative net current contribution with a smaller absolute value due to the negative gradient of the function $I_S(\xi)$ in that region.

The difference between the distribution in Figures 11a and 11b reveal the bulk flow velocity shear, which is absent in conventional Harris distributions. This is a key effect providing the embedded structure of TCSs supported by quasi-adiabatic Speiser orbits. This velocity shear effect is also clearly seen from the comparison of the current and plasma density plots in Figures 1b and 1c (in the vector-potential a-space), 2b and 2c (in the real space ζ).

7 TCS model in 2D

One of the main benefits of the developed analytical approximation of the SGS theory is the possibility of its immediate generalization to 2D. The corresponding TCS equilibria can be found by solving the original SGS system of equations (3)-(9) combined with (48) (M. I. Sitnov et al., 2007; M. I. Sitnov & Merkin, 2016).However, such numerical solutions are computationally expensive and difficult to analyze. In particular, it is difficult to investigate impacts of plasma anisotropy and current embedding on the TCS aspect ratio. Here we propose a simplified description of 2D TCS equilibria taking into account three small parameters of the problem, $\varepsilon_1 = B_z(x,0)/B_0$, $|\delta_1|$ and δ_2, which reflect strong tail stretching, weak plasma anisotropy and strong embedding ($L_{TCS} \ll L_H$). We start from the 2D isotropic Harris solution with thickness $L_H \gg 1$, that is the CS is much thicker than the thermal ion gyroradius. Its ion distribution will be Maxwellian with the anisotropic modification (58). Then we neglect the correction to the normal magnetic field B_z, because it is already a small parameter. The correction of the field B_x in the form (56) includes rescaling its thickness parameter $\delta_2(x) = \delta_2/\beta(x)$ and its asymptotic value, the lobe magnetic field B_0, which becomes now a function of x, following the the embedding Harris solution (e.g. M. I. Sitnov & Schindler, 2010): $B_0(x) = B_0/\beta(x)$ where the function β is determined by the magnetic field stretching factor $L\beta'/\beta = \varepsilon_1$.

It is important here that, in contrast to the Harris thickness parameter L_H, which grows as $L\beta(x)$, and does it very rapidly if the initial half-thickness L is small (e.g., $L \sim \rho_{0i}$), the TCS thickness $L_{TCS} \sim \rho_{0i}$ grows much slower in the case of strong embedding $L \gg \rho_{0i}$. As follows from (M. I. Sitnov & Merkin, 2016, Eq. (24)), in the region of weak anisotropy its scaling ratio

$$\frac{L_{TCS}}{L_{xTCS}} \sim \frac{\rho_{0i}}{L}\frac{L}{L_{xTCS}} \sim \frac{\rho_{0i}}{L}\frac{LB_0'}{B_0} \sim \delta_2\varepsilon_1 \tag{65}$$

This estimate shows that the TCS thickness scaling along the tail has an additional small parameter, compared to the Harris theory, the embedding factor $\delta_2 \ll 1$. At the same time, the estimate (65) suggests that the TCS aspect ratio in the region of weak anisotropy, being drastically different from its analog in the isotropic (Harris) limit $L_z/L_x \sim \varepsilon_1$, does not depend on the anisotropy strength determined by the parameter δ_1.

These estimates are confirmed by Figures 12 and 13 obtained using a 2D generalization of (56). In Figure 12 we compare the 2D TCS model with the parameters $\delta_1 = 0.2$ and $\delta_2 = 0.125$ (Figure 12a) with two 2D Harris-type models with $\delta_2 = 0.25$ and 0.125.(Figures 12b and 12c). The comparison of Figures 12a and 12b with comparable current sheet thickness values at the left boundary of the box (note that, according to Figure 2c, the TCS thickness $> \rho_{\perp 0i}$) shows that the TCS models have indeed much larger aspect ratios compared to Harris solutions, even in case of a weak anisotropy. The comparison of Figures 12a and 12c shows that the ion-scale TCS (Figure 12a) embedded into a thicker Harris sheet (Figure 12c) keeps the x-scale of the latter, even though the TCS is much thinner ($\delta_2 = 0.125$). The dotted field lines in Figure 12a, which are built based on the embedding thicker Harris sheet solution (Figure 12c) show that the TCS solution deviates from the corresponding Harris solution in the region $|z| \lesssim \rho_{\perp 0i}$. One more important distinction of the 2D TCS solution seen in Figure 12a is that the field lines do not coincide with the iso-contours of the current density as is the case for Harris models (Figures 12b and 12c).

Figure 13 compares different 2D TCS models to reveal their dependence on the parameters ε_1, δ_1 and δ_2. In particular, Figures 13a and 13b confirm that, consistent with the estimate (65), the TCS aspect ratio weakly depends on the specific value of the plasma anisotropy δ_1 as long as it is weak. According to these figures, a reduction of anisotropy rather reduces the TCS current density peak. At the same time, according to Figure 13c, a reduction of the embedding strength (due to an increase of the parameter δ_2) reduces

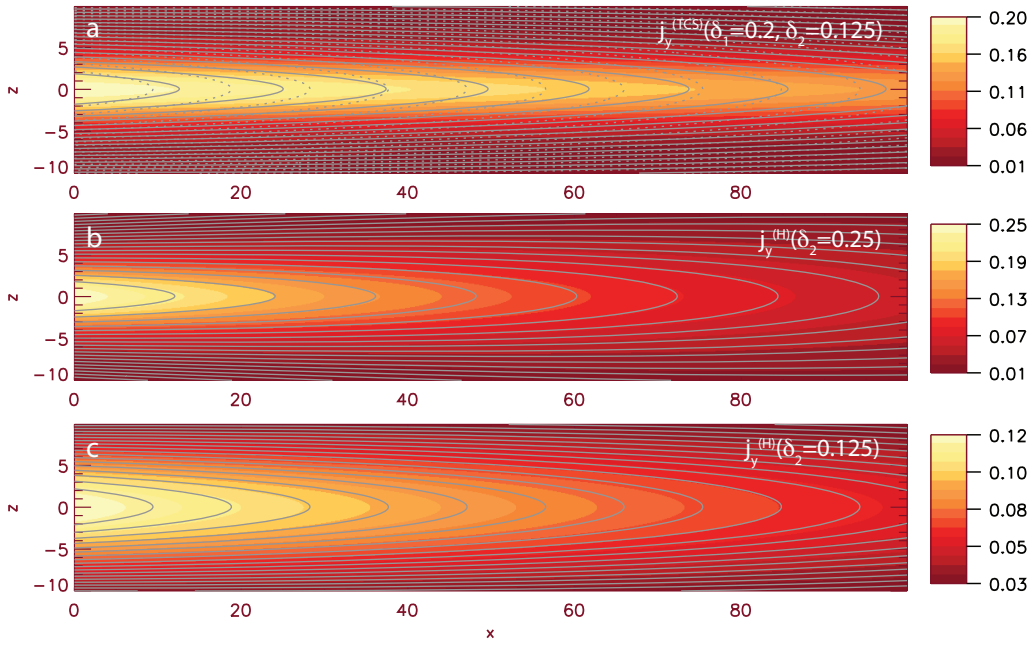

Figure 12. Current density distributions and field lines (grey color) for three 2D current sheet models with $\varepsilon_1 = 0.03$: (a) Weakly anisotropic TCS model based on Eq.(56) with the anisotropy and embedding parameters $\delta_1 = 0.2$ and $\delta_2 = 0.125$; (b)-(c) Harris-type models with $\delta_2 = 0.25$ and 0.125. Note that in case of Harris the parameter δ_2 is just a ratio between the thermal ion gyroradius ρ_{0i} in the field B_0 and the current sheet thickness L. Grey dotted lines in panel (a) show the field lines similar to those shown in panel (c) but with a different constant for the corresponding vector potential (to make them closer to case (a) at the near-Earth boundary). Spatial coordinates are normalized by the ion gyroradius $\rho_{\perp 0i}$ based on the field B_0 at the left boundary of the box.

the aspect ratio L_{TCS}/L_{xTCS} quite substantially, consistent with (65). As is seen from Figure 13d, a similar effect is provided by the increase of the parameter ε_1, although it is expected from the corresponding 2D Harris theory (Schindler, 1972).

The TCS solution in Figure 12a can also be compared with recent empirical reconstructions of the multiscale tail current sheet structure (M. I. Sitnov et al., 2019; Stephens et al., 2019, 2022), an example of which is provided in Figure 14. In these reconstructions the multi-mission and multi-decade archives of the geomagnetic field data were mined to find k_{NN} events neighboring the event of interest in the space of global geomagnetic activity parameters, such as for instance, the storm and substorm indices SMR and SML provided by the SuperMag project (Gjerloev, 2012), as well as the solar wind electric field parameter (vB_z^{IMF}; where v is the solar wind speed and B_z^{IMF} is the north component of the Interplanetary Magnetic Field, IMF). The selection of the nearest neighbor subset, such that $1 \ll k_{NN} \ll k_{DM}$, where k_{DM} is the number of points in the archive ($k_{DM} \sim 10^7$, according to (Stephens et al., 2022)), provides both the strong selectivity of the reconstruction, which captures the proper phases of storms and substorms, and the abundance of data points available for the reconstruction of the spatial distributions of the magnetic field in space for the event of interest (with the typical value $k_{NN} = 32,000$). The latter feature allows one to use very flexible architectures of the magnetic field with arbitrary current distributions in the equatorial plane. Moreover, it becomes

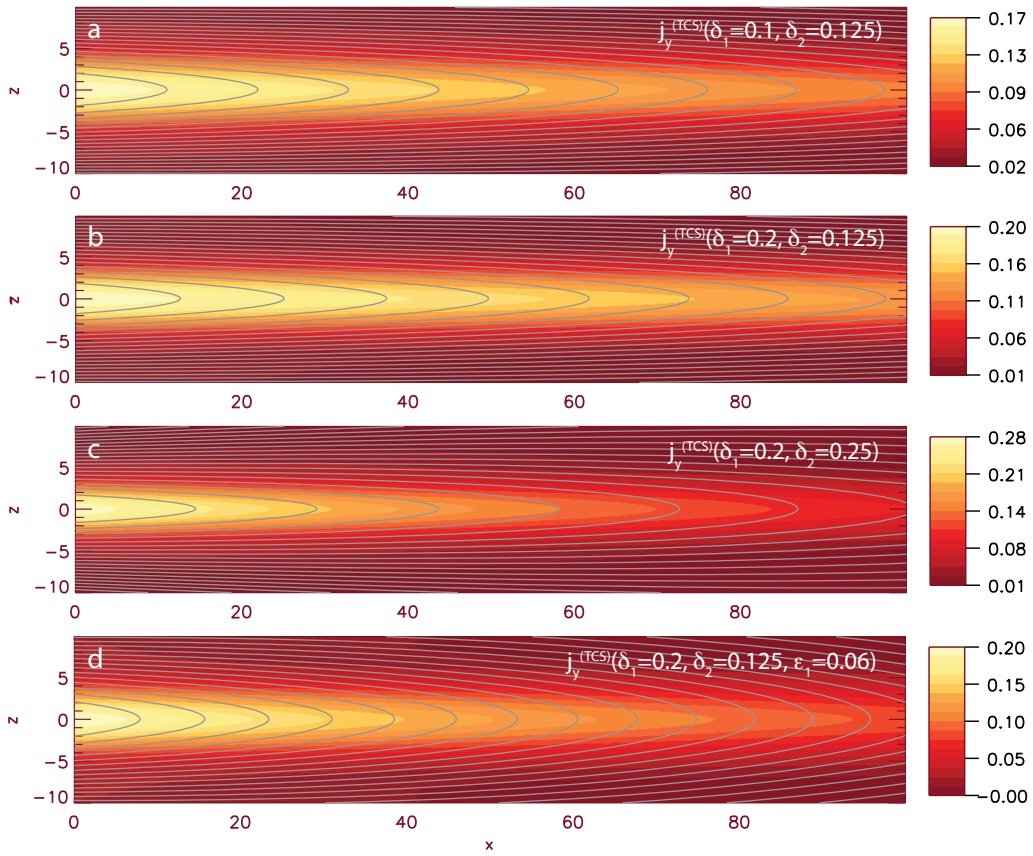

Figure 13. Current density distributions and field lines (grey color) for different 2D TCS models: (a)-(b) Weakly anisotropic TCS model based on Eq.(56) with $\varepsilon_1 = 0.03$, the anisotropy and embedding parameters $\delta_2 = 0.125$ and (a) $\delta_1 = 0.1$ and (b) $\delta_1 = 0.2$; (c) the analog of the model (b) but now with $\delta_2 = 0.25$; (d) the analog of the model (b) but now with $\varepsilon_1 = 0.06$.

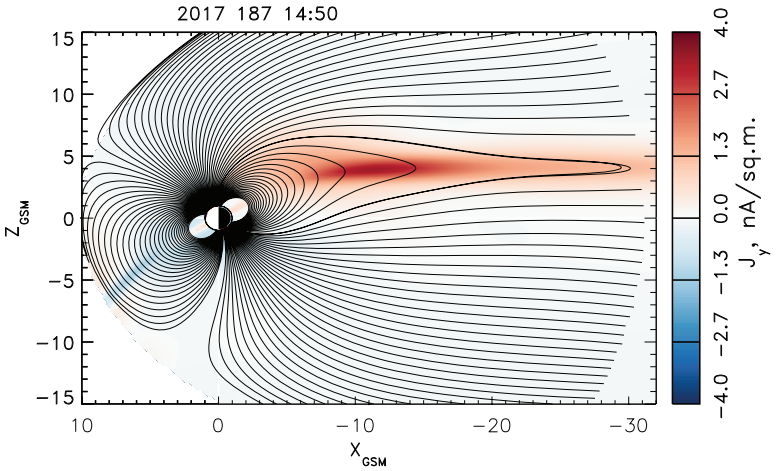

Figure 14. The current density distribution along the midnight meridian with overplotted (black) sample field lines obtained for the growth phase of the July 6 2017 substorm (14:50 UT) using the data mining method (M. I. Sitnov et al., 2019; Stephens et al., 2019, 2022) with the parameters $k_{NN} = 32,000$, $\sigma = 0.3$ and the magnetic field model architecture $(M, N) = (6, 8)$ and $N_{FAC} = 16$. The GSM coordinates are normalized by the Earth's radius $R_E = 6374$ km.

possible to resolve different equatorial distributions of the thick current sheet, whose thickness D is derived from fitting k_{NN} data, and the TCS with $D_{TCS} < D$.

In the most recent version of the reconstruction algorithm (Stephens et al., 2022), which was used to generate Figure 14, the possibility of the TCS scaling $D_{TCS} \sim B_L^{-1}$, where $B_L(\rho)$ is the lobe magnetic field depending on the distance ρ from the Earth (e.g. Wang et al., 2004), was provided by using the following approximation: $D_{TCS}(\rho) = [D_*^{-1} + \alpha \exp(-\beta\rho)]^{-1}$ with free parameters α, β and D_* to be inferred from data. The analysis by Stephens et al. (2022) confirmed that the scaling $D_{TCS} \propto B_L^{-1} \propto \rho_{Si}$ does indeed take place, which supports the theoretical mechanism of the TCS formation related to the Speiser orbits. Figure 14 shows the tail current sheet distribution, which is consistent with the present equilibrium theory: Similar to Figure 12a, it shows that the TCS ($D_{TCS} < 2.2R_E$) is embedded into a halo of the thicker current sheet ($D > 3R_E$) and the field lines do not coincide with the iso-contours of the current density. All mutiscale current sheet reconstructions (M. I. Sitnov et al., 2019; Stephens et al., 2019, 2022) suggest that $L_{TCS}/L_{xTCS} \ll B_z/B_L$, consistent with the present theory, and in particular, the estimate (65), as well as Figures 12a and 13.

8 Discussion

The final formulas of the weakly-anisotropic embedded TCS theory (56), (57), (58), (59), (61) and (62) demonstrate for the first time why the current density increase due to quasi-adiabatic ion motions may be substantial in spite of weak plasma anisotropy and they quantify this increase. Moreover, they make it possible for the first time to obtain in an explicit form and to systematically investigate the corresponding 2D TCS equilibria, and in particular, the impacts of plasma anisotropy, current sheet embedding and magnetic field line stretching on the aspect ratios of these equilibria.

The rather cumbersome calculations, which were necessary to derive the final set (56), (57), (58), (59), (61) and (62) of the weakly anisotropic TCS equilibrium theory, and which constitute this paper, require some further justification. Indeed, non-Harris TCS models, including 2D equilibria, are far more elaborated for generalizations of the

Harris model with the same or similar sets of integrals of motion, i.e., without the quasi-adiabatic invariant (1) (Schindler & Birn, 2002; Birn et al., 2004; Camporeale & Lapenta, 2005; Balikhin & Gedalin, 2008). However, as is argued in section 2 on the example of the analysis (Schindler & Birn, 2002; Birn et al., 2004), these classical sets of invariants, the total energy and the canonical momentum $P_y(A_y(x,z))$, yield essentially the same isotropic force balance relationship $L_x/L_z \sim B_0/B_z$ (see section 2 for more detail), which is not supported by recent observations (Artemyev et al., 2015, 2016) and empirical reconstructions (M. I. Sitnov et al., 2019; Stephens et al., 2022, see also Figure 14).

The idea that special features of quasi-adiabatic Speiser orbits (Speiser, 1965) could explain the structure of thin ion-scale current sheets was formulated as long as fifty years ago (Eastwood, 1972; Hill, 1975; Francfort & Pellat, 1976). However, in spite of the derivation of the corresponding approximate invariant of motion (Schindler, 1965; Sonnerup, 1971; Büchner & Zelenyi, 1989), whose dependence on the vector potential was different from $P_y(A_y(x,z))$ due to the integration along the the particle orbits, it was not implemented in the selfconsistent equilibrium theory for almost three decades, likely because of the extreme complexity of the underlying quasi-adiabatic dynamics (e.g. Büchner & Zelenyi, 1989).

The first self-consistent quasiadiabatic ion TCS theory was developed by Kropotkin et al. (1997) who used a simplified form of the invariant (1) suitable in the limit of strong plasma anisotropy outside TCS. Later M. I. Sitnov et al. (2000) generalized the TCS theory making it suitable for an arbitrary value of the ion temperature anisotropy by using the general definition of the invariant (1). While that theory described the 2D equilibria with the finite value of the northward magnetic field B_z, it did that for homogeneous in x models with $L_x \to \infty$, because the quasiadiabatic invariant (1) replaced $P_y(A_y(x,z))$. Note that the corresponding eigenvalue of the 2000 TCS theory coincided with the marginal firehose condition $P_{||0} - P_{\perp 0} = B_0^2/4\pi$ (Cowley, 1978; Burkhart et al., 1992a, $P_{||0}$ and $P_{\perp 0}$ are the parallel and perpendicular ion pressures outside TCS) when the magnetic tension force is balanced by the ion inertia rather than by the pressure gradient. Yet, that 2000 TCS theory could not describe more realistic tail equilibria with weak plasma anisotropy, because it simply had no isotropic (Harris) limit in the absence of the original canonical momentum $P_y(A_y(x,z))$ in the distribution functions.

The transition to the Harris limit has only become possible in the SGS model (M. I. Sitnov et al., 2003), whose ion distribution combined the quasiadiabatic invariant I_z and the canonical momentum P_y. And even in that model the obtaining of a concise analytical description in the limit of weak anisotropy turned out to be quite challenging. One of the reasons is the singular behavior of the small embedding parameter $\delta_2 \ll 1$, which enters the denominators of the corrections in (35), (56) and (57), and which required to verify the adopted assumptions, such as the small role of the electrostatic effects, numerically, using exact solutions of the original SGS system of equations. Another reason has become the necessity to retain terms $O(\delta_1\delta_2)$ in (24) and (25) that play key roles in the proper description of the magnetic field correction in its depression region outside TCS ($a \gtrsim 3$ in Figure 7). Finally, the presentation of the TCS distribution function required different descriptions of the distribution types for orbits crossing the neutral plane $z = 0$ (61) and those not crossing it (62), consistent with the invariant description in (Schindler, 1965; Sonnerup, 1971; Büchner & Zelenyi, 1989).

9 Conclusion and Outlook

The model described above is the first step on the way toward a new generation of thin current sheet models with multiscale structure and moderate plasma anisotropy. It is an analytical approximation of the SGS model (M. I. Sitnov et al., 2003) taking explicitly into account the unusual features of the ion Speiser motions, which were qualitatively described before (see, for instance, (L. M. Zelenyi et al., 1990) or (Zelenyĭ et

al., 2003, Fig. 3)): The parts of the Speiser orbits that cross the neutral plane $B_x = 0$ may create a substantial paramagnetic current contribution on the scales of these orbits, in contrast to conventional Larmor circles of their non-crossing parts whose contribution is diamagnetic. Here we show that the corresponding current enhancement on the scale of the ion gyroradius (Figures 1c, 2c and 3) may be substantial even in the case of small plasma anisotropy outside the TCS. This is seen in particular from the comparison of the relative perturbations of the plasma and current densities (47) and (35).

The main equation (56) in our new theory is a direct generalization of the hyperbolic tangent magnetic field formula in the classical Harris theory (Harris, 1962, Eq.(20)), now with an important capability to take into account weak anisotropy of the ion species and the possible agyrotropic effects of quasi-adiabatic (Speiser) orbits of ions. Note that, while the main formula (56) of our theory has been elaborated with applications to embedded TCSs, it can also be applied to describe bifurcated TCSs (e.g. Nakamura et al., 2002; Runov et al., 2003; V. Sergeev et al., 2003; Runov et al., 2005; Asano et al., 2005) in case of the negative values of the anisotropy parameter $\delta_1 = 1 - T_{\perp i}/T_{||i} < 0$ (M. I. Sitnov et al., 2003, 2004).

The impact of the quasi-adiabatic orbits is seen from the analysis in section 6, where their features are explicitly translated into the corresponding features of the ion distribution function, including the bulk flow velocity shear, diamagnetic and paramagnetic contributions to the electric current provided by the different regions of the ion orbits (Figure 10). The resulting description of the ion distribution function in terms of the elliptic integrals makes possible its efficient loading to modern particle codes such as P3D (Zeiler et al., 2002) using the rejection technique (e.g. Press et al., 1996).

Further investigations are necessary to clarify the mechanism of the pressure balance along the tail. Previous studies (Burkhart et al., 1992b) suggest that its description requires a further generalization of the quasi-adiabatic theory taking into account the finite value of the parameter B_z/B_0 and the corresponding bending of the Speiser orbits. Its details can also be clarified in PIC simulations starting from the 2D TCS equilibrium described in the previous section.

Another important next step should be taking into account the negative charging of TCSs and domination of electrons as current carriers. These features are suggested by observations (Asano et al., 2003; Artemyev et al., 2009). (Note that, as is seen from Figures 1d and 2d, the present model still reveals some CS charging effects. However, they are relatively small and they don not affect relative contributions of electron and ion currents.) They can be taken into account by changing the equation (9), which is an ad hoc assumption in the SGS theory to make it similar to the corresponding Harris theory assuming neutral current sheets. As was shown by (Yoon & Lui, 2004), in the case of isotropic models, the electron current domination can be provided by modifying (9) and using a small background plasma to eliminate the resulting electrostatic field at the current sheet boundary. The corresponding 2D models have recently been used in PIC simulations (M. I. Sitnov et al., 2021). The present investigation was limited by the Harris-like ion current dominated solutions to focus on the limit of the original 1962 Harris theory. We plan to investigate the effects of the TCS negative charging and electron domination in future studies.

Acknowledgments

The authors thank A. Artemyev and L. Zelenyi for useful discussions. This work was funded by NASA grants 80NSSC20K1271 and 80NSSC20K1787, as well as the NSF grant AGS-1744269. The analytical approximations provided in Eqs. (37), (40) and (55) have been obtained using the IDL code CURVEFIT (https://www.l3harrisgeospatial.com/docs/curvefit.html). The data used in the paper are archived on Zenodo (http://doi.org/10.5281/zenodo.7011514).

References

Abramowitz, M., & Stegun, I. A. (1964). *Handbook of mathematical functions with formulas, graphs, and mathematical tables* (ninth Dover printing, tenth GPO printing ed.). New York City: Dover.

Angelopoulos, V., Runov, A., Zhou, X.-Z., Turner, D. L., Kiehas, S. A., Li, S.-S., & Shinohara, I. (2013). Electromagnetic energy conversion at reconnection fronts. *Science*, *341*(6153), 1478–1482. doi: 10.1126/science.1236992

Artemyev, A. V., Angelopoulos, V., & Runov, A. (2016). On the radial force balance in the quiet time magnetotail current sheet. *Journal of Geophysical Research: Space Physics*, *121*(5), 4017-4026. doi: https://doi.org/10.1002/2016JA022480

Artemyev, A. V., Angelopoulos, V., Vasko, I. Y., Zhang, X.-J., Runov, A., & Zelenyi, L. M. (2019). Ion anisotropy in Earth's magnetotail current sheet: Multicomponent ion population. *Journal of Geophysical Research: Space Physics*, *124*(5), 3454-3467. doi: 10.1029/2019JA026604

Artemyev, A. V., Petrukovich, A. A., Nakamura, R., & Zelenyi, L. M. (2015). Two-dimensional configuration of the magnetotail current sheet: THEMIS observations. *Geophysical Research Letters*, *42*(10), 3662-3667. doi: https://doi.org/10.1002/2015GL063994

Artemyev, A. V., Petrukovich, A. A., Zelenyi, L. M., Nakamura, R., Malova, H. V., & Popov, V. Y. (2009). Thin embedded current sheets: Cluster observations of ion kinetic structure and analytical models. *Annales Geophysicae*, *27*(10), 4075–4087. Retrieved from `https://angeo.copernicus.org/articles/27/4075/2009/` doi: 10.5194/angeo-27-4075-2009

Asano, Y., Mukai, T., Hoshino, M., Saito, Y., Hayakawa, H., & Nagai, T. (2003). Evolution of the thin current sheet in a substorm observed by Geotail. *Journal of Geophysical Research: Space Physics*, *108*(A5). doi: 10.1029/2002JA009785

Asano, Y., Nakamura, R., Baumjohann, W., Runov, A., Vörös, Z., Volwerk, M., ... Rème, H. (2005). How typical are atypical current sheets? *Geophysical Research Letters*, *32*(3). doi: 10.1029/2004GL021834

Balikhin, M., & Gedalin, M. (2008). Generalization of the Harris current sheet model for non-relativistic, relativistic and pair plasmas. *Journal of Plasma Physics*, *74*(6), 749763. doi: 10.1017/S002237780800723X

Bessho, N., & Bhattacharjee, A. (2014). Instability of the current sheet in the Earth's magnetotail with normal magnetic field. *Phys. Plasmas*, *21*(1), 102905.

Birn, J., Schindler, K., & Hesse, M. (2004). Thin electron current sheets and their relation to auroral potentials. *Journal of Geophysical Research: Space Physics*, *109*(A2). doi: https://doi.org/10.1029/2003JA010303

Büchner, J., & Zelenyi, L. M. (1989). Regular and chaotic charged particle motion in magnetotaillike field reversals: 1. Basic theory of trapped motion. *Journal of Geophysical Research: Space Physics*, *94*(A9), 11821-11842. doi: https://doi.org/10.1029/JA094iA09p11821

Burkhart, G. R., Drake, J. F., Dusenbery, P. B., & Speiser, T. W. (1992a). Ion tearing in a magnetotail configuration with an embedded thin current sheet. *Journal of Geophysical Research: Space Physics*, *97*(A11), 16749-16756. doi:

https://doi.org/10.1029/92JA01523

Burkhart, G. R., Drake, J. F., Dusenbery, P. B., & Speiser, T. W. (1992b). A particle model for magnetotail neutral sheet equilibria. *Journal of Geophysical Research: Space Physics*, *97*(A9), 13799-13815. doi: https://doi.org/10.1029/92JA00495

Camporeale, E., & Lapenta, G. (2005). Model of bifurcated current sheets in the Earth's magnetotail: Equilibrium and stability. *Journal of Geophysical Research: Space Physics*, *110*(A7). doi: https://doi.org/10.1029/2004JA010779

Cole, G., & Schindler, K. (1972). On the equilibrium configuration of the geomagnetic tail. *Cosmic electrodynamics*, *3*, 275–284.

Coppi, B., Laval, G., & Pellat, R. (1966). Dynamics of the geomagnetic tail. *Physical Review Letters*, *16*(2), 1207–1210. doi: 10.1103/PhysRevLett.16.1207

Cowley, S. (1978). The effect of pressure anisotropy on the equilibrium structure of magnetic current sheets. *Planetary and Space Science*, *26*(11), 1037-1061. Retrieved from `https://www.sciencedirect.com/science/article/pii/0032063378900284` doi: https://doi.org/10.1016/0032-0633(78)90028-4

Eastwood, J. (1972). Consistency of fields and particle motion in the 'Speiser' model of the current sheet. *Planetary and Space Science*, *20*(10), 1555-1568. Retrieved from `https://www.sciencedirect.com/science/article/pii/0032063372901821` doi: https://doi.org/10.1016/0032-0633(72)90182-1

Francfort, P., & Pellat, R. (1976). Magnetic merging in collisionless plasmas. *Geophysical Research Letters*, *3*(8), 433-436. doi: https://doi.org/10.1029/GL003i008p00433

Galeev, A. A., & Zelenyi, L. M. (1976). Tearing instability in plasma configurations. *Zhurnal Eksperimentalnoi i Teoreticheskoi Fiziki*, *70*, 2133-2151.

Gjerloev, J. W. (2012). The SuperMAG data processing technique. *Journal of Geophysical Research: Space Physics*, *117*(A9), https://doi.org/10.1029/2012JA017683. doi: https://doi.org/10.1029/2012JA017683

Harris, E. (1962). On a plasma sheath separating regions of oppositely directed magnetic field. *Il Nuovo Cimento Series 10*, *23*(1), 115-121. Retrieved from `http://dx.doi.org/10.1007/BF02733547` doi: 10.1007/BF02733547

Hesse, M., & Schindler, K. (2001). The onset of magnetic reconnection in the magnetotail. *Earth, Planets and Space*, *53*, 645–653.

Hill, T. W. (1975). Magnetic merging in a collisionless plasma. *Journal of Geophysical Research (1896-1977)*, *80*(34), 4689-4699. Retrieved from `https://agupubs.onlinelibrary.wiley.com/doi/abs/10.1029/JA080i034p04689` doi: https://doi.org/10.1029/JA080i034p04689

Kropotkin, A. P., Malova, H. V., & Sitnov, M. I. (1997). Self-consistent structure of a thin anisotropic current sheet. *Journal of Geophysical Research: Space Physics*, *102*(A10), 22099-22106. doi: https://doi.org/10.1029/97JA01316

Lembege, B., & Pellat, R. (1982). Stability of a thick two-dimensional quasineutral sheet. *Phys. Fluids*, *25*, 1995–2004. doi: 10.1063/1.863677

Liu, Y.-H., Birn, J., Daughton, W., Hesse, M., & Schindler, K. (2014). Onset of reconnection in the near magnetotail: PIC simulations. *Journal of Geophysical Research: Space Physics*, *119*(12), 9773–9789. Retrieved from `http://dx.doi.org/10.1002/2014JA020492` doi: 10.1002/2014JA020492

Merkin, V. G., Panov, E. V., Sorathia, K. A., & Ukhorskiy, A. Y. (2019). Contribution of bursty bulk flows to the global dipolarization of the magnetotail during an isolated substorm. *Journal of Geophysical Research: Space Physics*, *124*(11), 8647-8668. doi: https://doi.org/10.1029/2019JA026872

Nagai, T., Fujimoto, M., Nakamura, R., Baumjohann, W., Ieda, A., Shinohara, I., ... Mukai, T. (2005). Solar wind control of the radial distance of the magnetic reconnection site in the magnetotail. *Journal of Geophysical Research: Space Physics*, *110*(A9). doi: https://doi.org/10.1029/2005JA011207

Nakamura, R., Baumjohann, W., Runov, A., Volwerk, M., Zhang, T. L., Klecker, B., ... Frey, H. U. (2002). Fast flow during current sheet thinning. *Geophysical Research Letters*, *29*(23), 55-1-55-4. doi: https://doi.org/10.1029/2002GL016200

NIST Digital Library of Mathematical Functions. (n.d.). http://dlmf.nist.gov/, Release 1.1.6 of 2022-06-30. Retrieved from `http://dlmf.nist.gov/` (F. W. J. Olver, A. B. Olde Daalhuis, D. W. Lozier, B. I. Schneider, R. F. Boisvert, C. W. Clark, B. R. Miller, B. V. Saunders, H. S. Cohl, and M. A. McClain, eds.)

Panov, E. V., & Pritchett, P. L. (2018). Ion cyclotron waves rippling ballooning/interchange instability heads. *Journal of Geophysical Research: Space Physics*, *123*(10), 8261-8274. doi: https://doi.org/10.1029/2018JA025603

Pellat, R., Coroniti, F. V., & Pritchett, P. L. (1991). Does ion tearing exist? *Geophys. Res. Lett.*, *18*, 143–146. doi: 10.1029/91GL00123

Press, W. H., Teukolsky, S. a., Vetterling, W. T., & Flannery, B. P. (1996). *Numerical Recipes in Fortran 77: the Art of Scientific Computing. Second Edition* (Vol. 1).

Pritchett, P. L. (2005). Externally driven magnetic reconnection in the presence of a normal magnetic field. *Journal of Geophysical Research: Space Physics*, *110*(A5), n/a–n/a. Retrieved from `http://dx.doi.org/10.1029/2004JA010948` doi: 10.1029/2004JA010948

Pritchett, P. L. (2010). Onset of magnetic reconnection in the presence of a normal magnetic field: Realistic ion to electron mass ratio. *Journal of Geophysical Research: Space Physics*, *115*(A10). doi: 10.1029/2010JA015371

Pritchett, P. L. (2015). Instability of current sheets with a localized accumulation of magnetic flux. *Physics of Plasmas*, *22*(6), -. Retrieved from `http://scitation.aip.org/content/aip/journal/pop/22/6/10.1063/1.4921666` doi: http://dx.doi.org/10.1063/1.4921666

Pritchett, P. L., & Coroniti, F. V. (2010). A kinetic ballooning/interchange instability in the magnetotail. *Journal of Geophysical Research: Space Physics*, *115*(A6). doi: https://doi.org/10.1029/2009JA014752

Rich, F. J., Vasyliunas, V. M., & Wolf, R. A. (1972). On the balance of stresses in the plasma sheet. *Journal of Geophysical Research (1896-1977)*, *77*(25), 4670-4676. doi: https://doi.org/10.1029/JA077i025p04670

Runov, A., Nakamura, R., Baumjohann, W., Zhang, T. L., Volwerk, M., Eichelberger, H.-U., & Balogh, A. (2003). Cluster observation of a bifurcated current sheet. *Geophysical Research Letters*, *30*(2). doi: https://doi.org/10.1029/2002GL016136

Runov, A., Sergeev, V. A., Baumjohann, W., Nakamura, R., Apatenkov, S., Asano, Y., ... Rème, H. (2005). Electric current and magnetic field geometry in flapping magnetotail current sheets. *Annales Geophysicae*, *23*(4), 1391–1403. Retrieved from `https://angeo.copernicus.org/articles/23/1391/2005/` doi: 10.5194/angeo-23-1391-2005

Runov, A., Sergeev, V. A., Nakamura, R., Baumjohann, W., Apatenkov, S., Asano, Y., ... Balogh, A. (2006). Local structure of the magnetotail current sheet: 2001 Cluster observations. *Annales Geophysicae*, *24*(1), 247-262. doi: 10.5194/angeo-24-247-2006

Schindler, K. (1965). Adiabatic particle orbits in discontinuous fields. *Journal of Mathematical Physics*, *6*(2), 313-321. doi: 10.1063/1.1704282

Schindler, K. (1972). A selfconsistent theory of the tail of the magnetosphere. In *Earth's Magnetospheric Processes, B.M. McCormac, ed.* (pp. 200–209). Dordrecht-Holland: D. Reidel.

Schindler, K. (1974). A theory of the substorm mechanism. *J. Geophys. Res.*, *79*(19), 2803–2810. doi: 10.1029/JA079i019p02803

Schindler, K., & Birn, J. (2002). Models of two-dimensional embedded thin current sheets from Vlasov theory. *Journal of Geophysical Research: Space Physics*, *107*(A8), SMP 20-1-SMP 20-13. doi: https://doi.org/10.1029/2001JA000304

Sergeev, V., Runov, A., Baumjohann, W., Nakamura, R., Zhang, T. L., Volwerk, M., ... Klecker, B. (2003). Current sheet flapping motion and structure observed by Cluster. *Geophysical Research Letters*, *30*(6). doi: https://doi.org/10.1029/2002GL016500

Sergeev, V. A., Angelopoulos, V., Kubyshkina, M., Donovan, E., Zhou, X.-Z., Runov, A., ... Nakamura, R. (2011). Substorm growth and expansion onset as observed with ideal ground-spacecraft THEMIS coverage. *J. Geophys. Res.*, *116*, A00I26. doi: 10.1029/2010JA015689

Sergeev, V. A., Mitchell, D. G., Russell, C. T., & Williams, D. J. (1993). Structure of the tail plasma/current sheet at $\sim 11R_E$ and its changes in the course of a substorm. *Journal of Geophysical Research: Space Physics*, *98*(A10), 17345-17365. doi: 10.1029/93JA01151

Sitnov, M., Birn, J., Ferdousi, B., Gordeev, E., Khotyaintsev, Y., Merkin, V., ... Zhou, X. (2019, 16). Explosive magnetotail activity. *Space Science Reviews*, *215*(4), 31. Retrieved from `https://doi.org/10.1007/s11214-019-0599-5` doi: 10.1007/s11214-019-0599-5

Sitnov, M. I., Buzulukova, N., Swisdak, M., Merkin, V. G., & Moore, T. E. (2013). Spontaneous formation of dipolarization fronts and reconnection onset in the magnetotail. *Geophys. Res. Lett.*, *40*(1), 22–27. doi: 10.1029/2012GL054701

Sitnov, M. I., Guzdar, P. N., & Swisdak, M. (2003). A model of the bifurcated current sheet. *Geophysical Research Letters*, *30*(13). doi: https://doi.org/10.1029/2003GL017218

Sitnov, M. I., Guzdar, P. N., & Swisdak, M. (2007). Atypical current sheets and plasma bubbles: A self-consistent kinetic model. *Geophysical Research Letters*, *34*(15). doi: https://doi.org/10.1029/2007GL029693

Sitnov, M. I., & Merkin, V. G. (2016). Generalized magnetotail equilibria: Effects of the dipole field, thin current sheets, and magnetic flux accumulation. *Journal of Geophysical Research: Space Physics*, *121*(8), 7664–7683. Retrieved from `http://dx.doi.org/10.1002/2016JA023001` doi: 10.1002/2016JA023001

Sitnov, M. I., Merkin, V. G., Pritchett, P. L., & Swisdak, M. (2017). Distinctive features of internally driven magnetotail reconnection. *Geophysical Research Letters*, *44*(7), 3028-3037. doi: 10.1002/2017GL072784

Sitnov, M. I., Merkin, V. G., Swisdak, M., Motoba, T., Buzulukova, N., Moore, T. E., ... Ohtani, S. (2014). Magnetic reconnection, buoyancy, and flapping motions in magnetotail explosions. *Journal of Geophysical Research: Space Physics*, *119*(9), 7151-7168. doi: 10.1002/2014JA020205

Sitnov, M. I., Motoba, T., & Swisdak, M. (2021). Multiscale nature of the magnetotail reconnection onset. *Geophysical Research Letters*, *48*(10), e2021GL093065. doi: https://doi.org/10.1029/2021GL093065

Sitnov, M. I., & Schindler, K. (2010). Tearing stability of a multiscale magnetotail current sheet. *Geophys. Res. Lett.*, *37*, 08102. doi: 10.1029/2010GL042961

Sitnov, M. I., Stephens, G. K., Tsyganenko, N. A., Miyashita, Y., Merkin, V. G., Motoba, T., ... Genestreti, K. J. (2019). Signatures of nonideal plasma evolution during substorms obtained by mining multimission magnetometer data. *Journal of Geophysical Research: Space Physics*, *124*(11), 8427-8456. doi: 10.1029/2019JA027037

Sitnov, M. I., Swisdak, M., Drake, J. F., Guzdar, P. N., & Rogers, B. N. (2004). A model of the bifurcated current sheet: 2. Flapping motions. *Geophysical Research Letters*, *31*(9). doi: https://doi.org/10.1029/2004GL019473

Sitnov, M. I., Swisdak, M., Guzdar, P. N., & Runov, A. (2006). Structure and dynamics of a new class of thin current sheets. *Journal of Geophysical Research: Space Physics*, *111*(A8). doi: https://doi.org/10.1029/2005JA011517

Sitnov, M. I., Zelenyi, L. M., Malova, H. V., & Sharma, A. S. (2000). Thin current sheet embedded within a thicker plasma sheet: Self-consistent kinetic theory. *Journal of Geophysical Research: Space Physics*, *105*(A6), 13029-13043. doi: https://doi.org/10.1029/1999JA000431

Sonnerup, B. U. O. (1971). Adiabatic particle orbits in a magnetic null sheet. *Journal of Geophysical Research (1896-1977)*, *76*(34), 8211-8222. doi: https://doi.org/10.1029/JA076i034p08211

Speiser, T. W. (1965). Particle trajectories in model current sheets: 1. Analytical solutions. *Journal of Geophysical Research (1896-1977)*, *70*(17), 4219-4226. doi: https://doi.org/10.1029/JZ070i017p04219

Stephens, G. K., Sitnov, M. I., Korth, H., Tsyganenko, N. A., Ohtani, S., Gkioulidou, M., & Ukhorskiy, A. Y. (2019). Global empirical picture of magnetospheric substorms inferred from multimission magnetometer data. *Journal of Geophysical Research: Space Physics*, *124*(0). Retrieved from `https://agupubs.onlinelibrary.wiley.com/doi/abs/10.1029/2018JA025843` doi: 10.1029/2018JA025843

Stephens, G. K., Sitnov, M. I., Weigel, R. S., Turner, D. I., Tsyganenko, N. A., Rogers, A. J., ... Slavin, J. A. (2022). Global structure of magnetotail reconnection revealed by mining space magnetometer data. *Earth and Space Science Open Archive*. doi: 10.1002/essoar.10511996.1

Torbert, R. B., Burch, J. L., Phan, T. D., Hesse, M., Argall, M. R., Shuster, J., ... Saito, Y. (2018). Electron-scale dynamics of the diffusion region during symmetric magnetic reconnection in space. *Science*, *362*(6421), 1391–1395. doi: 10.1126/science.aat2998

Walsh, A. P., Owen, C. J., Fazakerley, A. N., Forsyth, C., & Dandouras, I. (2011). Average magnetotail electron and proton pitch angle distributions from Cluster PEACE and CIS observations. *Geophysical Research Letters*, *38*(6). doi: 10.1029/2011GL046770

Wang, C.-P., Lyons, L. R., Nagai, T., & Samson, J. C. (2004, December). Midnight radial profiles of the quiet and growth-phase plasma sheet: The Geotail observations. *J. Geophys. Res. Space Phys.*, *109*(A), 12201. doi: 10.1029/2004JA010590

Yoon, P. H., & Lui, A. T. Y. (2004). Model of ion- or electron-dominated current sheet. *Journal of Geophysical Research: Space Physics*, *109*(A11). doi: 10.1029/2004JA010555

Zeiler, A., Biskamp, D., Drake, J. F., Rogers, B. N., Shay, M. A., & Scholer, M. (2002). Three-dimensional particle simulations of collisionless magnetic reconnection. *J. Geophys. Res.*, *107*(A), 1230. doi: 10.1029/2001JA000287

Zelenyi, L., Artemiev, A., Malova, H., & Popov, V. (2008). Marginal stability of thin current sheets in the Earth's magnetotail. *J. Atm. Sol.-Terr. Phys.*, *70*(2–4), 325–333. doi: 10.1016/j.jastp.2007.08.019

Zelenyi, L. M., Galeev, A. A., & Kennel, C. F. (1990). Ion precipitation from the inner plasma sheet due to stochastic diffusion. *Journal of Geophysical Research: Space Physics*, *95*(A4), 3871-3882. doi: https://doi.org/10.1029/JA095iA04p03871

Zelenyi, L. M., Malova, H. V., Popov, V. Y., Delcourt, D., & Sharma, A. S. (2004). Nonlinear equilibrium structure of thin currents sheets: influence of electron pressure anisotropy. *Nonlinear Processes in Geophysics*, *11*(5/6), 579–587. Retrieved from `https://npg.copernicus.org/articles/11/579/2004/` doi: 10.5194/npg-11-579-2004

Zelenyĭ, L. M., Malova, H. V., & Popov, V. Y. (2003, September). Splitting of thin current sheets in the Earth's magnetosphere. *Soviet Journal of Experimental and Theoretical Physics Letters*, *78*(5), 296-299. doi: 10.1134/1.1625728